NSU Florida
NOVA SOUTHEASTERN UNIVERSITY

Nova Southeastern University
NSUWorks

All HCAS Student Capstones, Theses, and Dissertations

HCAS Student Theses and Dissertations

12-7-2023

Investigating the Effects of a Southward Flow in the Southeastern Florida Shelf Using Robotic Instruments

Alfredo Quezada
Nova Southeastern University

Follow this and additional works at: https://nsuworks.nova.edu/hcas_etd_all

 Part of the Environmental Indicators and Impact Assessment Commons, Environmental Monitoring Commons, Fluid Dynamics Commons, Oceanography Commons, Other Earth Sciences Commons, and the Statistical Methodology Commons

Share Feedback About This Item

NSUWorks Citation

Alfredo Quezada. 2023. *Investigating the Effects of a Southward Flow in the Southeastern Florida Shelf Using Robotic Instruments.* Master's thesis. Nova Southeastern University. Retrieved from NSUWorks, . (159)
https://nsuworks.nova.edu/hcas_etd_all/159.

This Thesis is brought to you by the HCAS Student Theses and Dissertations at NSUWorks. It has been accepted for inclusion in All HCAS Student Capstones, Theses, and Dissertations by an authorized administrator of NSUWorks. For more information, please contact nsuworks@nova.edu.

Thesis of
Alfredo Quezada

Submitted in Partial Fulfillment of the Requirements for the Degree of

Master of Science
Marine Science

Nova Southeastern University
Halmos College of Arts and Sciences

December 2023

Approved:
Thesis Committee

Committee Chair: Alexander Soloviev, Ph.D.

Committee Member: Richard E. Dodge, Ph.D.

Committee Member: Ye Tao, Ph.D.

This thesis is available at NSUWorks: https://nsuworks.nova.edu/hcas_etd_all/159

NOVA SOUTHEATERN UNIVERSITY

HALMOS COLLEGE OF ARTS AND SCIENCES

Investigating the Effects of a Southward Flow in the Southeastern Florida Shelf Using Robotic Instruments

By

Alfredo Quezada

Submitted to the Faculty of
Halmos College of Arts and Sciences
in partial fulfillment of the requirements for
the degree of Master of Science with a specialty in:

Marine Science

Nova Southeastern University

December 2023

Abstract

We deployed a Slocum G3 glider fitted with an acoustic Doppler current profiler (ADCP), a Conductivity-Temperature-Depth sensor (CTD), optics sensor channels, and a propeller on the Southeastern Florida shelf. The ADCP and CTD provide continuous measurements of Northern and Eastern current velocity components, salinity, temperature, and density, throughout the water column in a high-current environment. The optics sensor channels are able to provide measurements of chlorophyll concentrations, colored dissolved organic matter (CDOM), and backscatter particle counts. Additionally, for one of the glider deployments, we deployed a Wirewalker wave-powered profiling platform system also fitted with an ADCP and a CTD in the vicinity of the glider's area for intercalibration of the devices. As the glider's velocity profiles are analyzed through time and space we saw evidence of an intermittent southward flow (SWF) opposite to the overlying northward Florida Current (FC) that was previously described by Soloviev et al. (2017). Meandering and strength of this SWF was influenced by the presence or absence of the Gulf Stream close to the shore, persisting in time spans of at least a few hours. Although specific mechanisms that influence the SWF's behavior are still unknown, our results show that its attachment to the shore along the continental slope was associated with the presence of eddy features in some sort of coupled system with possible implications on turbulent mixing. CTD results show that the SWF appears as either an undercurrent or a countercurrent depending on the strength of the water column stratification. Optical channel results show that the SWF assists in the southwards transport of particulate matter and biological material at depth, with possible implications on nutrient transport and biological activity. Richardson number results for analysis of turbulent flow were inconclusive as to how much turbulence is actually created by the SWF, but it does show evidence of increased turbulent activity at the interface between the SWF and the FC during some deployments. Analysis of the relationship between the northern component of velocity and the eastern component revealed a possible mechanism that would provide the optimal conditions for upwelling events to take place. 23 deployments have been done so far, with more planned for the future. More research is needed to accurately assess the effect the SWF has on velocities and transport of pollution and biological material along and across the shelf against the FC.

Keywords: Glider, Wirewalker, ADCP, CTD, Optics, Florida, Currents, Gulf Stream, Seasonality, Eddies, Richardson Number

Acknowledgements

I want to thank my committee members Alexander Soloviev, Richard Dodge, and Ye Tao, for their support and useful commentary throughout this project. I also want to thank my lab mates John Kluge, Stephanie Ball, Terry Thompson, Geoffrey Morrison, and Brian Ettinger for their mentorship, support, and friendship over the last two years.

I want to thank and make a special mention to Megan Miller and Breanna Vanderplow for being great friends without whom I wouldn't have been able to do this and for helping me keep myself sane and healthy.

I wish to thank our collaborators and sponsors for their useful discussion and allowing this project to take place in the first place. I want to greatly thank Andreas M. Thurnherr for his comments on the research and providing us with the LADCP processing procedure that made this research possible. This work has been supported by the ONR Awards N00014-18-1-2835, N00014-21-1-4007, N00014-22-1-2008, N00014-23-1-2270, and N00014-23-1-2746. Any opinions, findings and conclusions or recommendations expressed in this material are those of the author(s) and do not necessarily reflect the views of the U.S. Navy. The views expressed in this article are those of the author and do not necessarily reflect the official policy or position of the Department of the Navy, Department of Defense, nor the U.S. Government.

Finally, I want to thank my close friends and family for their love and support throughout this entire journey. My parents, my brothers, and my friends from back home who I am not able to see as much as I'd like, but who I still love and appreciate very much.

Table of Contents

1. List of Figures VI

2. List of Tables IX

3. Introduction 1

I. The Florida Current (FC) 1

II. The Southward Flow 3

III. Oceanographic Instruments 4

i. Autonomous Underwater Vehicles (AUVs): The Glider and the Wirewalker 4

ii. Sensors 10

4. Statement of Purpose 10

5. Materials and Methods 11

I. Deployment Site and Data Collection 11

II. Platform Motion-Correction for Velocities 14

III. Data Processing and Analysis 16

i. ADCP Measurements 16

ii. CTD Measurements 17

iii. Validation of Velocity Measurements 17

iv. Optics Figures 18

v. 3D Figures 18

vi. Ruchardson Number 19

vii. Statistical Analyses 19

6. Results 20

I. Current Velocities and Direction 20

II. CTD Measurements 25

III. Intercalibration of Instrumentation 27

IV. Optical Measurements 30
V. 3D Figures and Eddies 32
VI. Turbulence 35
VII. Upwelling 37
7. Discussion 39
I. Intercalibration of Instruments 39
II. General Observations of the SWF 41
III. Temperature, Salinity, and Density 44
IV. Transport of Particulates and Biological Material 45
V. Eddy Activity 47
VI. Turbulent Flow 47
VII. Upwelling 48
8. Conclusions 51
9. Limitations and Future Steps 52
10. References 54
11. Appendix A: Glider ADCP Figures 59
12. Appendix B: Glider CTD Figures 61
13. Appendix C: Glider Optics Figures 63
14. Appendix D: Glider Richardson Figures 65
15. Appendix E: Tables 66

1. List of Figures

Figure 1. Schematic of the Loop Current System in the Gulf of Mexico. The Loop Current enters the Gulf of Mexico as the Yucatan Current and exits as the Florida Current through the Florida Straits. The map also shows two states of the Loop Current, a retracted and an extended state. An example of an eddy shed by the Loop Current during its extended state is also shown (Credit UCAR & NASA; Dortch, 2018).
Figure 2. Schematic of the SWF (yellow) attached to the continental slope of the southeastern Florida shelf. The northwards flowing Florida Current (purple) is also shown for comparison (Credit Soloviev et al., 2017).
Figure 3. The Slocum G3 glider owned by NSU's Physical Oceanography Laboratory and used for this study's deployments.
Figure 4. An example of a typical glider profiling track. While at the surface, the glider can communicate with the pilot to receive new coordinates if necessary, and so adjust the path of the next dive (Credit Zhang et al., 2020).
Figure 5. The Wirewalker system visualized. This is the standard system provided by Del Mar Oceanographic. Additionally, the system used in this study attached the down-weights to a concrete anchor to prevent it from floating away (Credit Del Mar Oceanographic, LLC).
Figure 6. Schematic of how the Wirewalker uses surface wave energy to move downwards along the profiling wire (Credit Del Mar Oceanographic, LLC).
Figure 7. Our Wirewalker free-floating during a deployment.
Figure 8. Map of glider and Wirewalker approximate deployment locations. The two waypoints inside the red rectangle are the approximate locations where the glider was deployed during the 2022-2023 missions (northern waypoint), and the Wirewalker was deployed during the one intercalibration mission (southern waypoint). For the deployment where both the glider and Wirewalker were deployed, the glider constantly travelled between these two waypoints while the Wirewalker was fixed to the southern waypoint. The red square is the location of NSU's Halmos College of Arts and Sciences.
Figure 9. The Slocum G3 glider with its instruments and propeller highlighted. Circled in red is the ADCP, circled in green is the CTD, and circled in orange is the propeller (Credit IKM 3D Animation Services).
Figure 10. The Wirewalker platform and its instruments. Circled in red is the ADCP, and circled in green is the CTD (Zheng et al., 2022).
Figure 11. Example profile of one dive from the glider June 10 – 13, 2023 deployment. The LADCP procedure automatically matches the East and North components of the LADCP velocities, represented by the red and blue profiles, to the bottom tracking components observed by the ADCP, represented by the green and black profiles.
Figure 12. Example of non-corrected and corrected Wirewalker current velocity components for one of the upcasts. Raw East and North, the red and blue profiles, are without the motion and tilt correction. East and North correction, the green and black profiles, have already been motion and tilt corrected.

Figure 13. Google Earth view of all the available glider deployment tracks. Deployments began offshore of Fort Lauderdale, 16 km north of the entrance to Port Everglades, Florida, and 8-12 km offshore. Style of track chosen for each deployment varied for either data collection or testing purposes.

Figure 14. Examples of LADCP contours for current direction, left column, and north component of velocity, right column. Current direction was calculated from east and north components of current velocity. Note that depth changes as time advances (white background). This is due to the glider moving across and along the shelf. Shallower depths represent dives when the glider was close to the shore, while deeper depths represent when the glider was offshore. Values of direction go from -180° to 180°, with ±180° being absolute SWF (dark blue), and 0° being absolute northward flow (dark red). Values for northern velocity go from -0.8 m/s (dark blue) to 1.4 m/s (dark red), with 0 m/s represented by a light cyan coloring and negative values representing the SWF. Each contour pair (i.e. each row) represents a different deployment throughout the 2022 seasons. As such, the 14A and 14B deployment occurred during the spring, the 14C and 14D deployment occurred during the summer, the 14E and 14F deployment occurred during the fall, and the 14G and 14H deployment occurred during the winter.

Figure 15. Example CTD color contours for two different deployments. Contours on the left column (15A, 15B, and 15C) correspond to a deployment that occurred during the summer season of 2022. Contours on the right column (15D, 15E, and 15F) correspond to a deployment that occurred during the winter season of 2022.

Figure 16. CTD measurement contours. Contours on the left column (16A, 16B, and 16C) are from the Wirewalker, while contours on the right column (16D, 16E, and 16F) are from the glider. The contours are from a deployment where both instruments were in the ocean at the same time and in the vicinity of each other. Note that the seafloor is variable in the glider contours due to navigation of the instrument between two waypoints, while it is relatively constant in the Wirewalker contours due to its movement being restricted to the vertical direction only.

Figure 17. Contours of the components of velocities for the Wirewalker (17A and 17B) and the glider (17C and 17D).

Figure 18. Example optical channels color contours for two different deployments. Contours on the left column (15A, 15B, and 15C) correspond to a deployment that occurred during the summer season of 2022. Contours on the right column (15D, 15E, and 15F) correspond to a deployment that occurred during the winter season of 2022.

Figure 19. Examples of different 3D plots. Contours 19A and 19B correspond to a deployment that occurred during the summer of 2022 and the SWF was missing. Contours 19C and 19D correspond to a deployment that occurred during fall of 2022 and the SWF was present as an undercurrent. Contours 19E and 19F correspond to a deployment that occurred during the winter of 2022 and the SWF was present as an undercurrent at first, and then as a countercurrent. The plots on the right column are the same as the contours on the left column, but plotted with glider

tracking as well to facilitate the visualization of movement across and along the shelf. Local bottom topography is also included. Vectors in these plots are for the 20 m depth bin.

Figure 20. Velocity contour for the northern component of the current throughout time and depth and a vector plot showing overall current direction. Vectors provided for the 20 m depth bin. Contour is for glider deployment that occurred on 10-11 October 2022. 20B is a graphic highlighting the eddy-like feature observed from the vector plot in 20A.

Figure 21. Example of Richardson number contours from the 3 deployments presented in Figure 19. Contours 19A and 19B correspond to a deployment that occurred during the summer of 2022 and the SWF was missing. Contours 19C and 19D correspond to a deployment that occurred during fall of 2022 and the SWF was present as an undercurrent. Contours 19E and 19F correspond to a deployment that occurred during the winter of 2022 and the SWF was present as an undercurrent at first, and then as a countercurrent. The contours on the right column only portray Richardson numbers that were below the critical value of 0.3 to easily visualize where critical values were reached and overturning of the water column occurred.

Figure 22. CTD and optical channels contours from the glider for the deployment used during the Wirewalker intercalibration

Figure 23. Averaged eastern and northern velocity components for the deployments when the SWF appeared as an undercurrent. The dashed black lines are the respective 0 m/s value for both components.

2. List of Tables

Table 1. Correlation analysis results for the detection of possible upwelling. 5 different scenarios are taken into consideration and color coded: data from all deployments (blue), data from deployments where the southward flow was minimal or completely absent (green), data from deployments where the southward flow was prominent as either an undercurrent or a countercurrent (orange), data from deployments where the southward flow appeared as an undercurrent (red), and data from deployments where the southward flow appeared as a countercurrent (purple). Variable 1 is represented by north velocity in all 5 different scenarios, variable 2 is each different variable it was tested against for all 5 different scenarios. If the p-value was extremely small, the program outputted a 0 for its value.

3. Introduction

I. The Florida Current (FC)

The predecessor of the Florida Current (FC), the Loop Current, forms in the Gulf of Mexico as a result of water from the western boundary current of the North Atlantic subtropical gyre piling up due to the rotation of the Earth and entering the Gulf through the Yucatan Channel (Candela et al., 2002; Perez-Brunius et al., 2018). In the Gulf, the current flows clockwise creating large and energetic eddies before exiting through the Straits of Florida, where it becomes the FC and flows northwards along the eastern coast of the US into the North Atlantic as part of the Gulf Stream, as shown in Figure 1 (Oey et al., 2005; Otis et al., 2019; Perez-Brunius et al., 2018; Stommel, 1965). The FC depends highly on both spatial and temporal inhomogeneities of oceanic conditions, such as bottom topography, depth of the water column, meteorological variability, seasonal variability, etc. (Anderson & Corry, 1985; Kourafalou & Kang, 2012; Schott et al., 1988; Stommel, 1965; Zantopp et al., 1987). On average, the total steady-state volume transport of the FC is estimated to be about 30-32 Sv, with a variability of 2-10 Sv dependent on the time scale in consideration, at speeds of up to 2 m/s (Baringer & Larsen, 2001; Niiler & Richardson, 1973; Schmitz & Richardson, 1968). The FC also acts as an important mediator for biological activity, as it can be linked to several upwelling mechanisms, such as dynamic adjustments of the ocean due to variations in the FC (Smith, 1981), the passage of cyclonic eddies (Lee, 1975), and the delivery of offshore nutrient-rich water onto the continental shelf (Fiechter & Mooers, 2007).

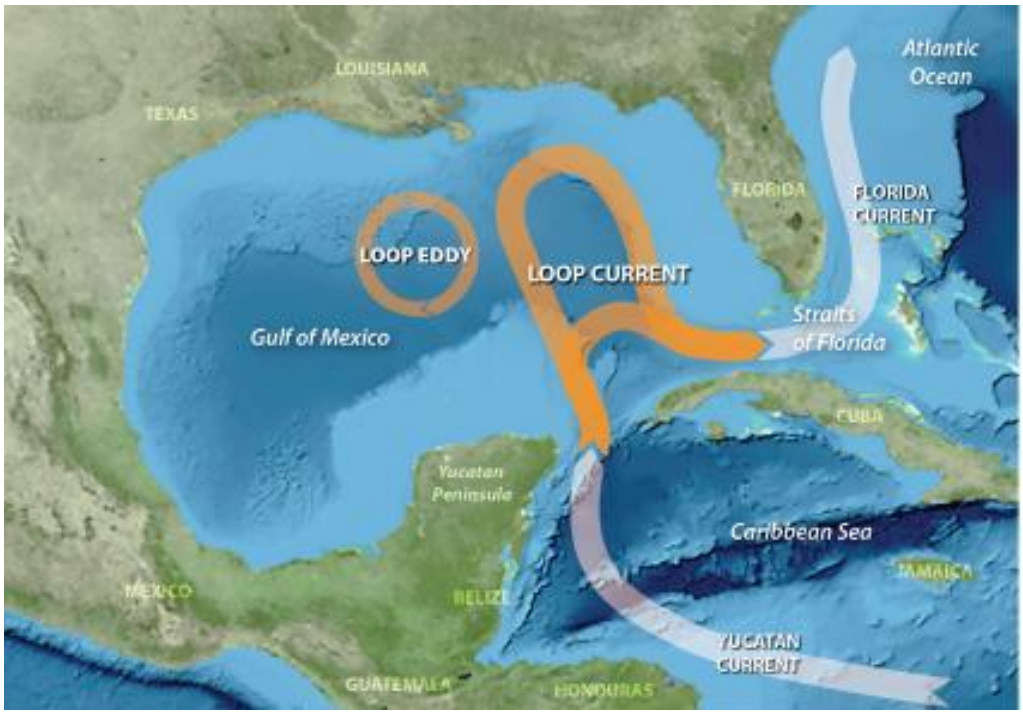

Figure 1. Schematic of the Loop Current System in the Gulf of Mexico. The Loop Current enters the Gulf of Mexico as the Yucatan Current and exits as the Florida Current through the Florida Straits. The map also shows two states of the Loop Current, a retracted and an extended state. An example of an eddy shed by the Loop Current during its extended state is also shown (Credit UCAR & NASA; Dortch, 2018).

One of the most well-known and important features associated with the FC is the appearance of eddies. Eddies are circular currents resulting from the divergence of the general current due to, for example, complex bottom topography, and are capable of transporting momentum, heat, mass, and chemical agents throughout the seawater (Chelton et al., 2007; Kourafalou & Kang, 2012; Robinson, 1983). Submesoscale eddies are those whose size is typically less than 10-20 km and their duration is on the order of hours to days (Ernst et al., 2023; Zhang & Qiu, 2020; Zhang et al., 2019). Previous studies in the southeastern Florida shelf have shown the consistent presence of cyclonic, anticlockwise, eddies that are not wind or tide induced (Kourafalou & Kang, 2012; Lee, 1975; Zhang et al., 2019). These eddies are most likely formed through interactions between the FC and topography, or they have traveled northward and eastward from the original formation location at the exit of the Gulf of Mexico (Kourafalou & Kang, 2012; Zhang et al., 2019). The counterclockwise rotation of these eddies is also important for upwelling events. As such, eddies are important not only to the general oceanic circulation, but they also play an important role as modulators for nutrient transportation and biological activity

(Chelton et al., 2007; Robinson, 1983). Due to a combination of the rotation of the eddies and the Coriolis force, water is pushed away from the center of rotation, which then must be replaced by deep, cold, nutrient-rich waters to maintain equilibrium causing these events (Zhang & Qiu, 2020; Zhang et al., 2019). Additionally, in the southeastern Florida shelf, eddies are significantly important for the settlement and survival of coral reef fishes (Shulzitski et al., 2016; Sponaugle et al., 2005; Yeung et al., 2001). Depending on their scale, eddies can either be affected or affect the general circulation of the FC. It is therefore important to understand how eddy activity varies in both space and time to more accurately assess their effects on coastal circulation of the southeastern Florida shelf.

II. The Southward Flow

The Southward Flow (SWF) on the Miami Terrace was previously reported by Soloviev et al. (2017), as shown in Figure 2. It was described as an intermittent flow attached to the continental slope of the southeastern Florida Shelf in the form of either an undercurrent or a countercurrent. Other studies also had sporadic observations of this SWF, but Soloviev et al. (2017) was the first attempt to obtain detailed observations on this specific flow on the western flank of the southeastern Florida Shelf (Duing & Johnson, 1971; Gardner et al., 1989; Leaman & Molinari, 1987; Soloviev et al., 2017). Their study reported observations of the SWF in 3 distinct forms: as a seasonally dependent countercurrent, as an undercurrent attached to the continental slope, and as an intermittent undercurrent on the Miami Terrace. The SWF was found to vary seasonally in strength and location, while the exact mechanisms that drive its behavior are still unknown. Differences in speed, path, stratification, and depth between the SWF and the overlying FC due to seasonal variations might also have implications for turbulent mixing and zooplankton recruitment (Carr et al., 2008). The SWF has been observed to take the characteristics of an undercurrent during the summer and a countercurrent during the winter (Soloviev et al. 2017). To attempt to obtain detailed measurements of this flow's current strength, meandering, and impacts on other processes, different oceanographic instruments become important research tools.

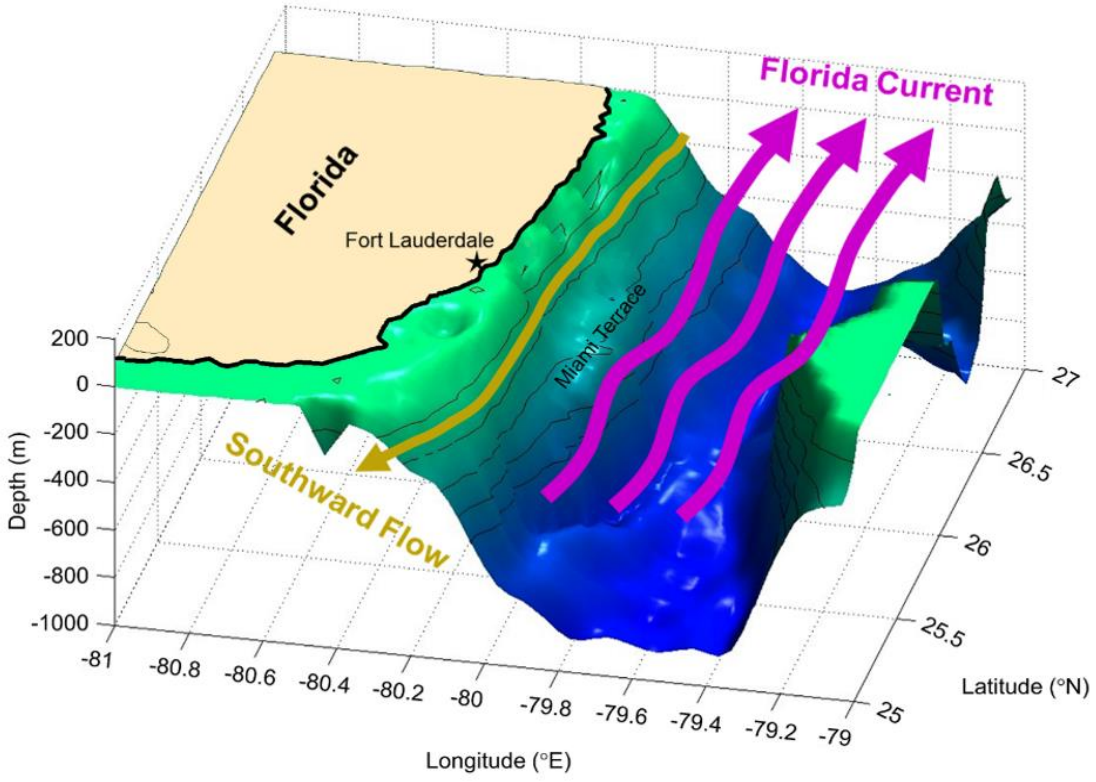

Figure 2. Schematic of the SWF (yellow) attached to the continental slope of the southeastern Florida shelf. The northwards flowing Florida Current (purple) is also shown for comparison (Credit Soloviev et al., 2017).

III. Oceanographic Instruments

i. Autonomous Underwater Vehicles (AUVs): The Glider and the Wirewalker

Autonomous Underwater Vehicles (AUVs) are robotic instruments used for their extensive applications for scientific research purposes, and a wide variety of other practical or theoretical fields (Gafurov & Klochkov, 2015; Sahoo et al., 2019). These instruments are unmanned and are preprogrammed to operate independently of the vessel from which they were deployed in time spans from several hours to weeks or months (Huvenne et al., 2017; Wynn et al., 2014). Their independence and lack of need to be tethered to a surface station therefore provides opportunities and accessibility to previously inaccessible parts of the ocean. AUVs have been used to explore oceanic environments ever since their creation in the late 1950s (Gafurov & Klochkov, 2015; Sahoo et al., 2019). Due to their ability of carrying a variety of sensor payloads, AUVs have a corresponding wide array of applications (Wynn et al., 2014). Some of their scientific

applications include, but are not limited to seafloor mapping, biological studies, geological and archaeological surveys, environmental monitoring, analyzing current environments, etc. (Sahoo et al., 2019). Their structural design has been classically inspired by submarines to resemble torpedoes, although many variations have been developed. Additionally, most, if not all, AUVs also depend on propulsion systems for effective underwater navigation.

Although AUVs are useful tools for scientific research, they also suffer from some limitations. For example, the lack of a physical tether to a surface or land-based station means they require an onboard power source not only for movement, but also for the equipped sensors (Huvenne et al., 2017). Untethered underwater communications also provide a challenge, since it means communicating with the AUV requires the instrument to either breach the surface or remain in the vicinity of the surface boat (Sahoo et al., 2019). While AUVs are a good instrument for acquiring sensor data along large spatial and temporal scales, their ROV counterparts (remotely operated underwater vehicles), which are tethered to a surface boat or land-based station, are better suited for precise, high-resolution, and highly detailed work (Huvenne et al., 2017; Ludvigsen et al., 2014). The use of either AUVs or ROVs for any given application should be assessed on a case-by-case basis. For the purpose of this study, two different types of AUVs were used: a glider and a Wirewalker.

Underwater gliders were developed as a result from a rising need for AUVs to remain underwater for extended periods of time for either scientific or military purposes (Gafurov & Klochkov, 2015). Gliders are torpedo shaped, with two wings on their side to maximize lift and a rear rudder to control turning movement (Gafurov & Klochkov, 2015; Javaid et al., 2014; Rudnick, 2016). Glider profiling occurs in a “saw-tooth” like pattern through a change in buoyancy of the instrument that drives it up or down the water column as needed (Gafurov & Klochkov, 2015). The buoyancy change is achieved by the pumping of oil into and out of an internal bladder to an external one, thus changing vehicle volume but keeping mass constant, affecting the overall buoyancy and pitch (Gafurov & Klochkov, 2015; Javaid et al., 2014; Rudnick, 2016). For this study, a Slocum G3 glider was used, as shown in Figure 3, and an example of a typical glider profiling trajectory is shown by Figure 4. Due to the high-current-activity nature of our study area, our glider also uses a propulsion system with a propeller mounted at its rear to allow for proper navigation and minimize risk of instrument loss.

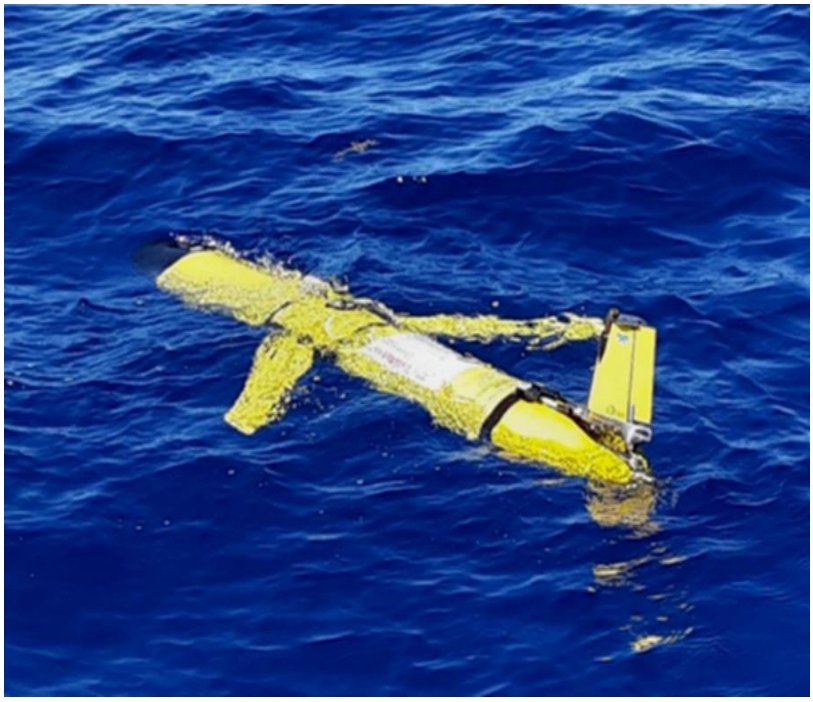

Figure 3. The Slocum G3 glider owned by NSU's Physical Oceanography Laboratory and used for this study's deployments.

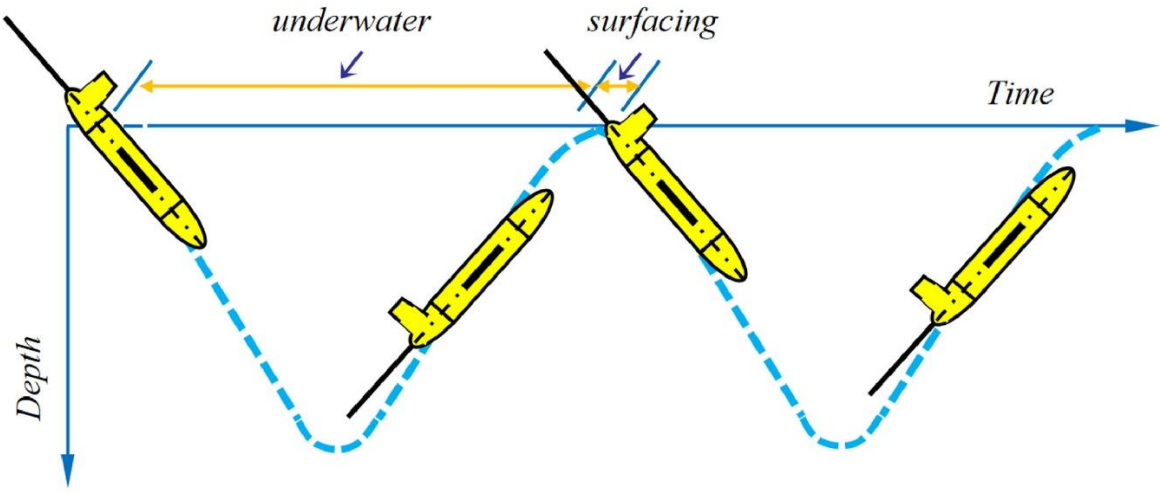

Figure 4. An example of a typical glider profiling track. While at the surface, the glider can communicate with the pilot to receive new coordinates if necessary, and so adjust the path of the next dive (Credit Zhang et al., 2020).

The Wirewalker is a different type of AUV. It functions as a profiling platform to which several recording instruments may be attached to obtain different types of measurements throughout the water column (Pinkel et al., 2011). The system itself is comprised of a surface

buoy to which a wire with a mechanical stop at both ends is attached and held down by counterweights at depth, as shown in Figure 5 (Pinkel et al., 2011; Rainville & Pinkel, 2001). There are two modes for this system: free drifting, where the system is not physically attached to a single location, or anchored, where the counterweights are connected to a seafloor anchor to prevent the system from drifting away (Pinkel et al., 2011). In this study an anchored system is used. The system works by taking advantage of the difference in vertical motion between surface waters and water at depth, and uses wave energy to move the platform downward along a wire (Pinkel et al., 2011; Smith et al., 2011). The Wirewalker is positively buoyant and tends to float to the surface, but an internal one-way cam lock mechanism prevents it from moving up the wire until the lock is released (Pinkel et al., 2011; Rainville & Pinkel, 2001). As waves pass by the system and the buoy is lifted the Wirewalker slides down the wire, and once the buoy is returned to its initial position the Wirewalker remains fixed to its relative position on the wire, moving slightly downwards with each passing wave (Pinkel et al., 2011). Once the Wirewalker reaches the bottom, a mechanical stop causes the cam lock to release, allowing the platform to freely float to the surface while taking precise samplings throughout the water column (Pinkel et al., 2011; Rainville & Pinkel, 2001; Smith et al., 2011). Once it reaches the surface, another mechanical stop reactivates the cam lock, and the process is then repeated. This entire process can be visualized in Figure 6. The operational life of the instrument is dependent on both energy availability and material durability, but it can take continuous measurements for up to months at a time (Pinkel et al., 2011). Figure 7 shows our Wirewalker platform in action.

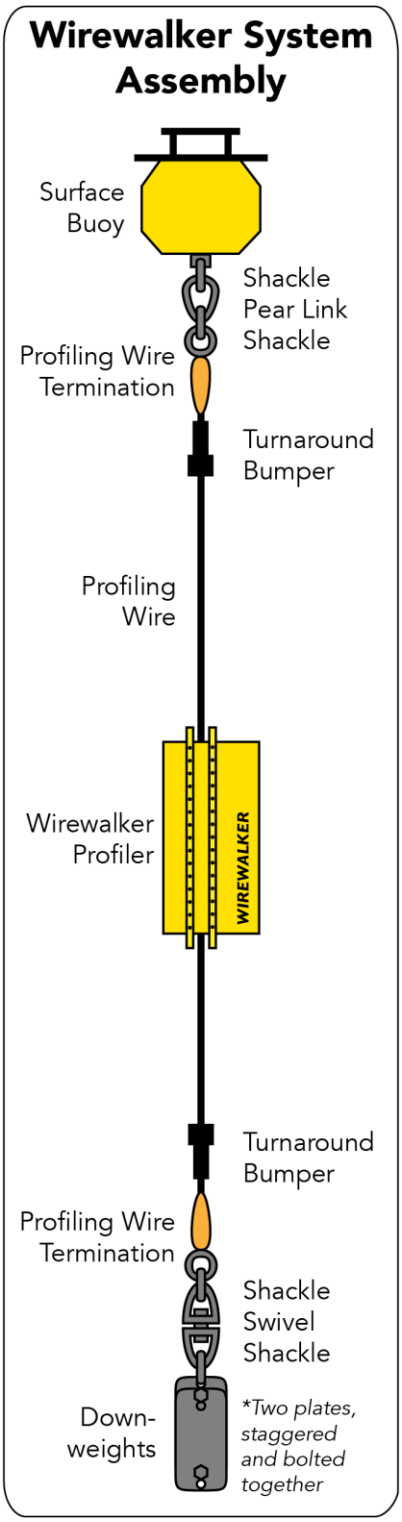

Figure 5. The Wirewalker system visualized. This is the standard system provided by Del Mar Oceanographic. Additionally, the system used in this study attached the down-weights to a concrete anchor to prevent it from floating away (Credit Del Mar Oceanographic, LLC).

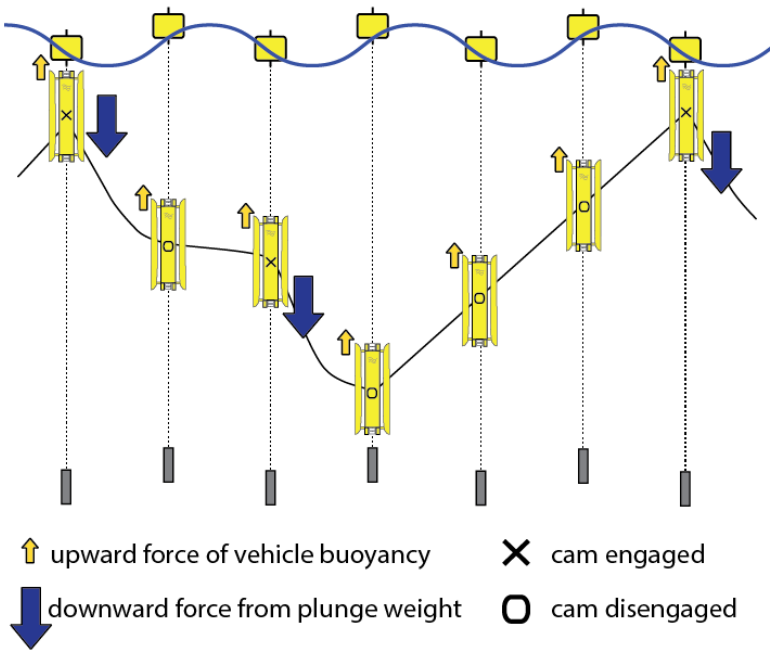

Figure 6. Schematic of how the Wirewalker uses surface wave energy to move downwards along the profiling wire (Credit Del Mar Oceanographic, LLC).

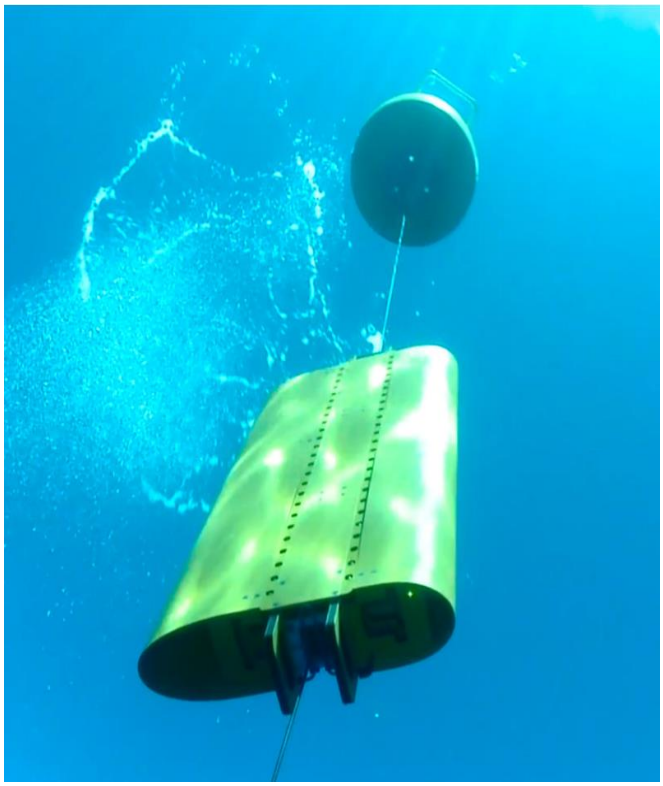

Figure 7. Our Wirewalker free-floating during a deployment.

ii. Sensors

Both the glider and the Wirewalker were fitted with an acoustic Doppler current profiler (ADCP) to obtain measurements of eastern and northern current velocity components. The ADCP works by using the principle of the Doppler Effect (Brumley et al. 1991). It measures shifts in frequency from when a sound wave "ping" is sent out and when it's echoed back to estimate current speed and direction in 3D space. ADCPs have been extensively used in the ocean to obtain current velocity measurements since the 1980s, and since then multiple advances in the area have been implemented to improve the device's accuracy and expand its functionality (Brumley et al., 1991; Gradone et al., 2021; Gotvald & Oberg, 2009; Ordonez et al., 2012; Pettigrew & Irish, 1983; Todd et al., 2017; Zheng et al., 2022).

Both instruments are also fitted with a Conductivity, Temperature, and Depth (CTD) sensor. The CTD allows us to obtain direct measurements of conductivity, temperature, and hydrostatic pressure, from which we can calculate salinity, density, and depth of the instrument at each time step (Brown & Morrison, 1978; Fofonoff & Millard 1983; Millero & Poisson 1981). CTDs are useful for providing accurate measurements of physical parameters of the ocean and have been widely used in oceanographic settings since the early 1970s (Brown, 1974; Brown & Morrison, 1978).

The glider is also fitted with optics channel sensors, which allow for the direct measurements of backscatter, colored dissolved organic matter (CDOM), and chlorophyll. These three parameters may serve as indicators of nutrient transport and presence or absence of biological activity. While the Wirewalker's ADCP can provide backscatter counts, we did not use these due to their poor accuracy when compared to the reliability of the glider's specialized sensors.

4. Statement of Purpose

The main objective of this project was to assess the changes in the activity of the SWF on the continental slope as the year progressed. I hope to find evidence that will help establish the spatiotemporal scales in which the SWF operates. I also hope to find how the SWF might affect the vertical distribution of particulates and biological material in the water column. I expect to observe an increase in coastal eddy activity whenever the SWF is present due to increased shear between itself and the FC, as previously hypothesized by Dr. Richard Dodge (Soloviev et al.,

2017). Finally, I also expect the SWF to significantly increase turbulent mixing and the southwards transport of cold, deep, nutrient-rich waters, possibly influencing or promoting upwelling events. Understanding the SWF variability and presence through time can provide insights into its own origin, other oceanic features' effects on its variability, possible turbulent mixing between itself and the overlying FC, and the mechanisms driving the observed patterns of ocean circulation. The comparison of the datasets from our different glider deployments throughout 2022 and 2023 could help provide an updated basis for the study of this SWF, its seasonal cycle, and its effects on other processes like the transport of nutrients, biological material, and pollutants.

5. Materials and Methods

I. Deployment Site and Data Collection

All glider deployments began roughly around the same area, 16 km north of the entrance to Port Everglades, Florida, and 8-12 km offshore, as pinpointed by the northern waypoint in Figure 8. The glider is able to continuously record measurements throughout the entire duration of each deployment. Deployments require no diving, but costs for boat access, materials, and time are covered by the grant. Limitations to deployments are restricted to availability of staff trained in glider deployment and monitoring, availability of the boat, and weather-permitting conditions. The deployment track is variable and actively modified remotely by the pilot depending on testing sites of interest, testing necessities, current strength, and to protect the device from other external hazards. Tracks varied in shape, but the three main types used were a straight line, snake-like, and a circular pattern. Recovery of the glider occurs when oceanic conditions allow, but deployments are planned for durations of roughly 24-48 hrs each. The ADCP mounted on the glider is a Teledyne RDI Explorer DVL set up at its default acoustic frequency of 614 kHz and sampling at 0.39 Hz. The ADCP is located on the bottom of the glider and is slanted forwards so that when the glider is diving the ADCP is directly facing the seafloor. The CTD mounted on the glider is a Sea-Bird Scientific Slocum Glider payload CTD sampling continuously at 1 Hz. It is located on the side of the glider. The location of these instruments and the propeller on the glider can be seen on Figure 9.

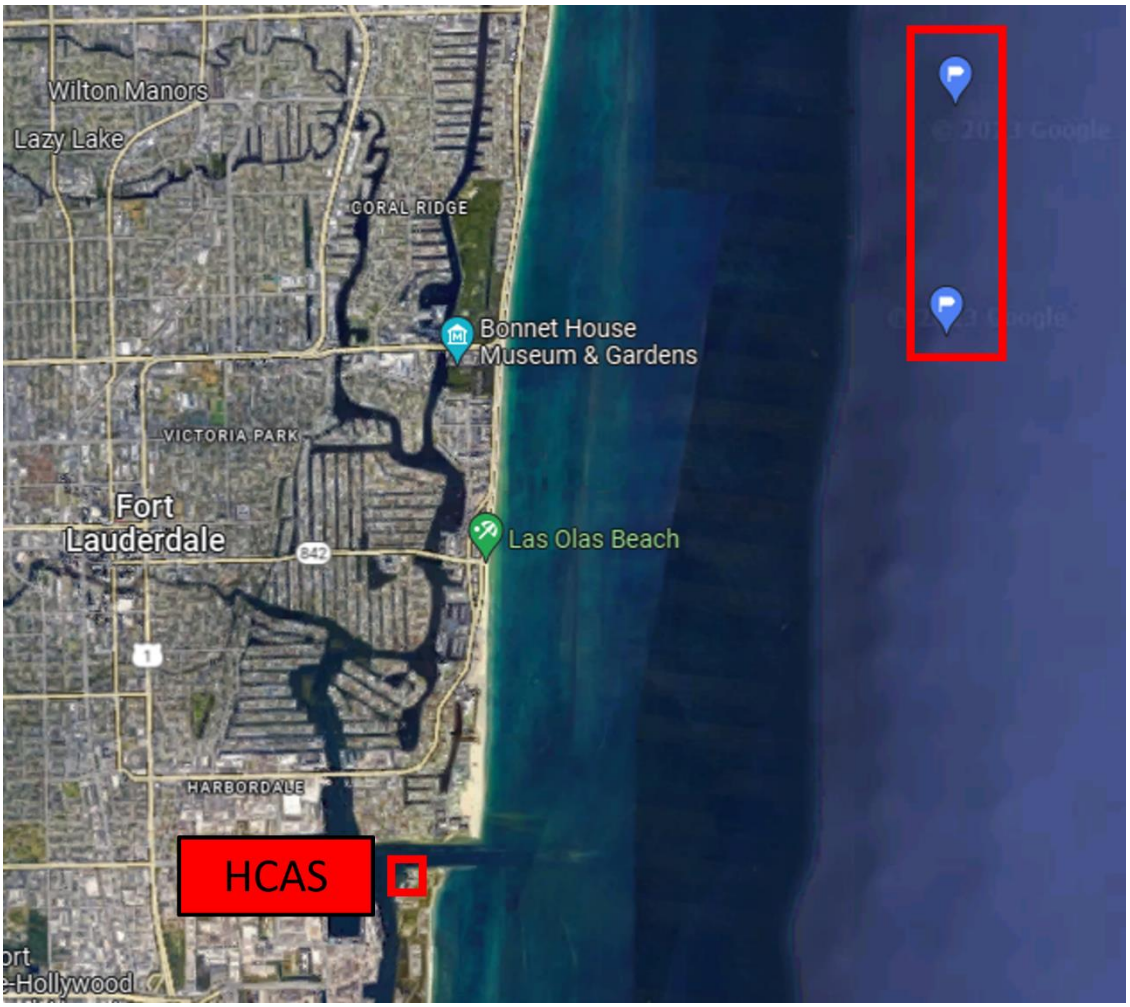

Figure 8. Map of glider and Wirewalker approximate deployment locations. The two waypoints inside the red rectangle are the approximate locations where the glider was deployed during the 2022-2023 missions (northern waypoint), and the Wirewalker was deployed during the one intercalibration mission (southern waypoint). For the deployment where both the glider and Wirewalker were deployed, the glider constantly travelled between these two waypoints while the Wirewalker was fixed to the southern waypoint. The red square is the location of NSU's Halmos College of Arts and Sciences.

Figure 9. The Slocum G3 glider with its instruments and propeller highlighted. Circled in red is the ADCP, circled in green is the CTD, and circled in orange is the propeller (Credit IKM 3D Animation Services).

Wirewalker deployments are always exactly in the same position, wherever the system is anchored. For the glider comparison, the system is located roughly 2 miles South of where the glider deployments usually begin, at the southern waypoint in Figure 8. Deployment of the Wirewalker requires diving and boat access. Limitations to deployments are restricted to availability of staff trained in Wirewalker deployment, staff with diver certifications, availability of the boat, and weather-permitting conditions. All costs for the deployment are covered by the grant. Deployments don't have to be continuously monitored due to the platform's ability to function exclusively with the use of wave energy and battery packs to allow for continuous measurements. Wirewalker deployments usually last around 1 week, but it can stay out in the field for months at a time. While the glider was deployed multiple times throughout 2022 and 2023, the Wirewalker was deployed a single time during June of 2022. For the comparison, and due to disastrous complications with the surface buoy, we are only able to use a 6-hour period for which we have data available for both the glider and Wirewalker. The ADCP mounted on the

Wirewalker is a Nortek Signature1000 set up at a frequency of 1229 kHz and in a 5-beam burst mode at a sampling frequency of 8 Hz. It is attached to the side of the platform and its central beam is pointing outwards horizontally. The CTD mounted on the Wirewalker is an RBRconcerto working at a sampling frequency of 6 Hz. The CTD is attached to the other side of the Wirewalker, but it's located within the casing of the platform. The platform and its instruments are shown in Figure 10.

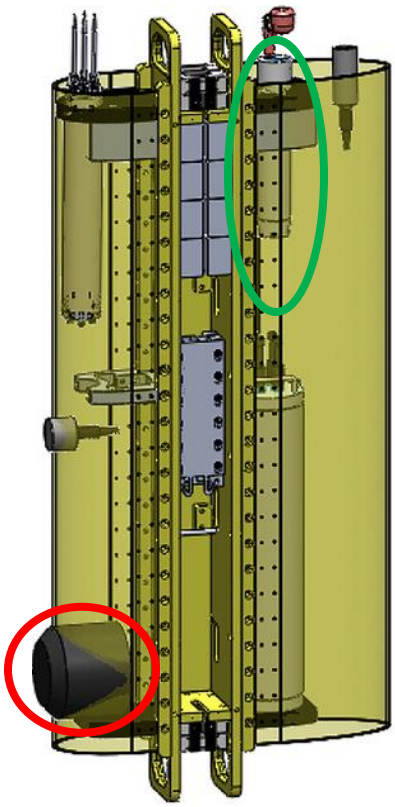

Figure 10. The Wirewalker platform and its instruments. Circled in red is the ADCP, and circled in green is the CTD (Zheng et al., 2022).

II. Platform Motion-Correction for Velocities

All data obtained from the ADCP and CTD are processed and plotted using Matlab. To correct for vehicle motion, glider velocity measurements were put through Thurnherr et al's (2015) Lowered Acoustic Doppler Current Profiler (LADCP) shear method procedure. This methodology provides profiles for both ADCP and bottom tracking velocities. The motion corrected ADCP profiles, now known as LADCP profiles, are calculated by taking into account the movement of the platform and direction the ADCP is pointing. The bottom tracking

measurements are obtained by the ADCP's ability to sense the seafloor to use as a reference for velocity estimates (Thurnherr et al., 2015). Bottom tracking profiles are only outputted for the first half of each dive, when the nose of the glider is pointing down and the ADCP is pointing directly at the seafloor. LADCP profiles are corrected to match bottom tracking profiles using a least squares fitting framework, providing accurate measurements throughout the entire water column. An example of how this looks on a plot is provided in Figure 11.

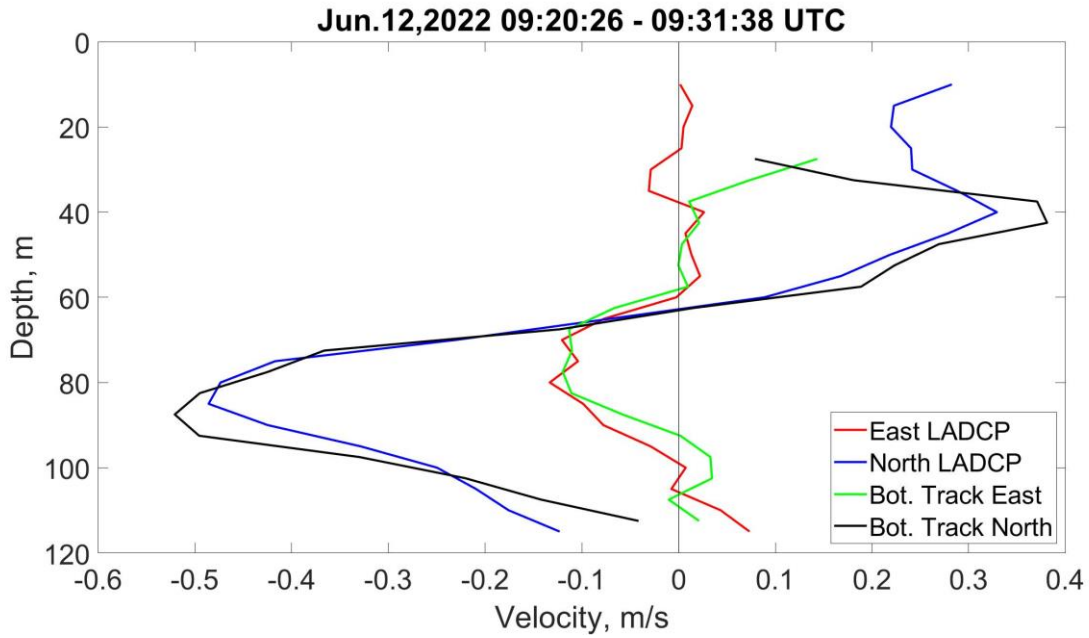

Figure 11. Example profile of one dive from the glider June 10 – 13, 2023 deployment. The LADCP procedure automatically matches the East and North components of the LADCP velocities, represented by the red and blue profiles, to the bottom tracking components observed by the ADCP, represented by the green and black profiles.

Wirewalker velocity measurements do not have a standardized procedure to correct for motion. Therefore, for every upcast and downcast pair the tilt associated with the cable of the system was calculated and components of North and East tilt were used to correct raw velocity measurements from the ADCP. By doing so, we are able to account for any noise in the measurements due to movement of the platform and tilt of the system due to high current. To keep it consistent with the glider profiles, Wirewalker velocities were also averaged every 5 m in the vertical direction. Figure 12 shows an example for a comparison between non-corrected and corrected profiles.

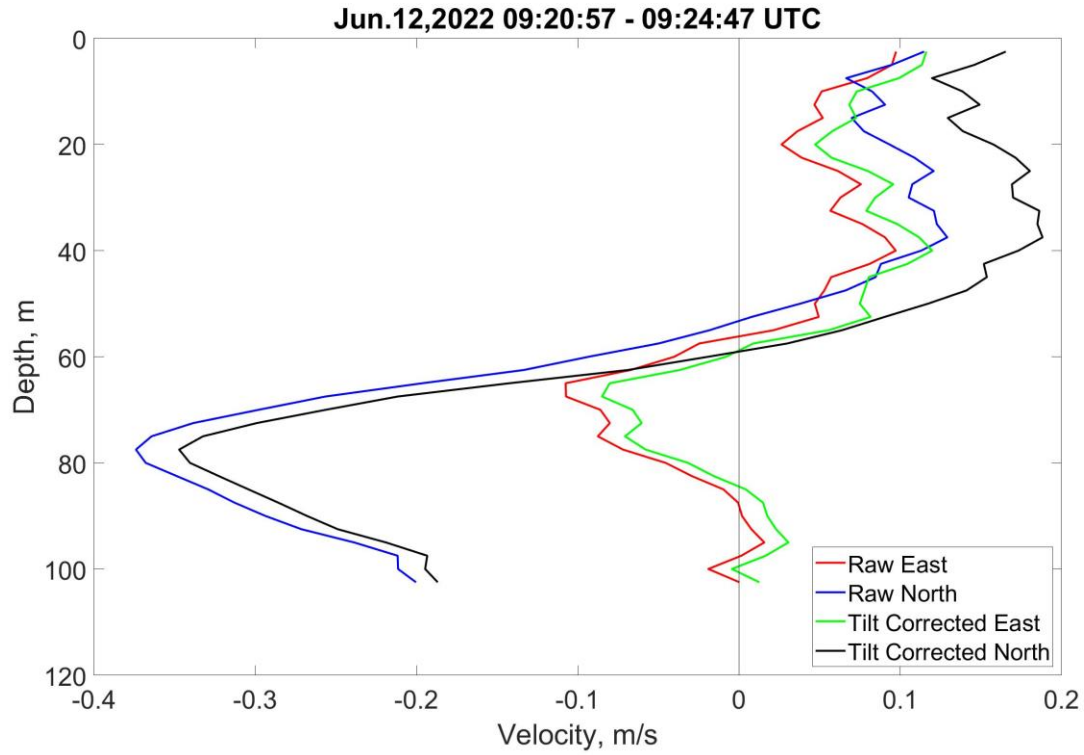

Figure 12. Example of non-corrected and corrected Wirewalker current velocity components for one of the upcasts. Raw East and North, the red and blue profiles, are without the motion and tilt correction. East and North correction, the green and black profiles, have already been motion and tilt corrected.

III. Data Processing and Analysis

i. ADCP Measurements

The glider LADCP procedure averages velocities every 5 m in the vertical direction by default, and that's the resolution used when plotting and analyzing all deployments. Given that the glider's ADCP is located below the vehicle, the LADCP profiles of velocity begin at the second depth bin (10 m depth). Not all dives provided accurate measurements. For some dive files, the methodology could not create bottom tracking profiles, resulting in erroneous LADCP velocity components. For those files, if the time range was small enough in comparison to the overall deployment time, data were interpolated in between to smooth the color contours. If the time between files where the blank zone was present was too large (i.e., more than an hour), then that section was left blank. The current direction was then calculated from the strength of the eastern and northern velocity components. For each individual glider dive, a plot of their

velocities was created for quality checking and backup purposes. Once done, all dives from their respective deployments were plotted together as a color contour to see changes through both time and space. Contours were created for bottom tracking East and North velocity components, LADCP East and North velocity components, and bottom tracking and LADCP current directions. To look for the presence of the SWF, current direction was analyzed, to look at current strength LADCP components were analyzed, and to quality check LADCP contours the bottom tracking components were analyzed.

As mentioned before, Wirewalker ADCP measurements were only available for a 6 hour period. For that dataset, only the upcasts were considered and color contours for the North and East velocity components were created to be compared against the glider dataset corresponding to the same time period. The reason only the upcasts were used is that when the platform is moving down the wire during the downcasts, it bounces up and down continuously which can create a lot of noise and alter results to reflect artificial current measurements. On the other hand, while the platform is free floating upwards during the upcasts, measurements are taken continuously without outside interference from the cam lock mechanism and minimizes the risk of tarnished results.

ii. CTD Measurements

The glider CTD provides measurements of temperature (°C), hydrostatic pressure (bars), and conductivity (conductivity ratio, unit-less), from which depth (m), salinity (PSU), and density (kg/m^3) are calculated. CTD measurements were averaged in the vertical direction every 0.25 m to create individual plots for each dive and overall contours for each deployment. For individual plots, averaging only occurs on the vertical direction. However, for the color contours, downcast and upcast measurements are averaged for each depth bin resulting in a single profile per dive to allow for interpolation. Wirewalker CTD measurements are similar to the ones provided by the glider CTD, and they are averaged every 0.25 m in the vertical direction and between each upcast and downcast pairs as well.

iii. Validation of Velocity Measurements

For the deployment where we had available data for both the glider and the Wirewalker, the glider constantly travelled between the two waypoints presented in Figure 8, while the Wirewalker was fixed to the southern waypoint. At their closest, the instruments were

approximately 100 m apart, at their farthest they were close to 2 km apart. For the intercalibration of the instruments, it is necessary to confirm that although the devices are not exactly together, they are still taking measurements of the same bodies of water. CTD measurements of temperature, salinity, and density can be used to confirm this. Therefore, both instruments' CTD and ADCP contours were compared side-by-side visually to assess the validity of CTD measurements and coherence between the velocity contours. Measurements of the same parameters were also compared through a Pearson correlation analysis to assess the strength of their association.

iv. Optics Figures

Optics channel measurements for the glider were processed similarly as the CTD measurements. The optics channel provides measurements of backscatter (no dimensions), colored dissolved organic matter (parts per billion, ppb), and chlorophyll (μg/L). Measurements were continuous throughout the entire deployment and, similar to the CTD, they were independent of ADCP measurements. Optics channel measurements were also averaged in the vertical direction every 0.25 m to create individual plots for each dive and overall contours for each deployment. For single dives, averaging only occurred in the vertical direction, and for the entire deployments' color contours, downcast and upcast measurements are averaged for each depth bin resulting in a single profile per dive to allow for interpolation. Optical figures were then compared to the glider's CTD and velocity contours.

v. 3D Figures

For all glider deployments, the number of dives varies between tens to hundreds. By also using dive and surface GPS coordinates, these dives can be plotted along a 3D representation of current velocities through time and space. The combination of all the dives into the 3D structure plot provides the same contours created before, but now changes through space are apparent, including the glider's pathing and distance from the shoreline. 3D plots were done for the northern component of current velocities to search for the presence of the SWF. 3D plots were also exclusive to glider deployments, as the glider is able to move freely through space, and due to the availability of multiple datasets throughout 2022 and 2023.

vi. Ruchardson Number

The Richardson number, Ri, is a dimensionless number that represents the ratio of the buoyancy term, the buoyant suppression of turbulence, to the shear term, the shear generation of turbulence. The number can be calculated as:

$$Ri = \frac{\frac{g}{\rho}\left(\frac{\delta\rho}{\delta z}\right)}{\left(\frac{\delta u}{\delta z}\right)^2 + \left(\frac{\delta v}{\delta z}\right)^2}, \tag{0.1}$$

where g is the gravitational acceleration, ρ is the density, z is the depth, and u and v are the horizontal velocity components. The Richardson number serves as an indicator for turbulence and mixing potential. Richardson number calculations were done using CTD-averaged measurements and LADCP-corrected measurements of velocity. CTD measurements were averaged in the vertical direction every 5 m to match velocity profiles, and Richardson number outputs were obtained for LADCP profiles of the glider deployments. Values below the chosen theoretical critical value of 0.3 signal intense turbulent mixing in the water column. No Richardson calculations have been done for the Wirewalker so far.

vii. Statistical Analyses

Pearson correlation coefficients (R) were obtained for several comparisons between variables to assess the strength of a linear relationship between them. First, the correlation coefficients for the temperatures, salinities, densities, and North velocities from the Wirewalker and the glider were calculated to aid in the validation of the intercalibration of the devices. CTD measurements from both instruments, and ADCP velocities from the Wirewalker, were averaged in the vertical to have matching depth bins with the glider. Glider velocities were then interpolated to match the Wirewalker, since it had more dives within the same amount of time. Second, correlation coefficients for all glider deployments were obtained for 5 distinct scenarios: all deployments, deployments where the southward flow was absent, when it was present, when it showed as an undercurrent, and when it showed as a countercurrent. This was done in order to determine if there were any significant relationships between variables of interest that might indicate the possibility of the presence of conditions that would allow upwelling events to occur, and if the SWF might have any association with the distribution of particulates and biological material.

6. Results

I. Current Velocities and Direction

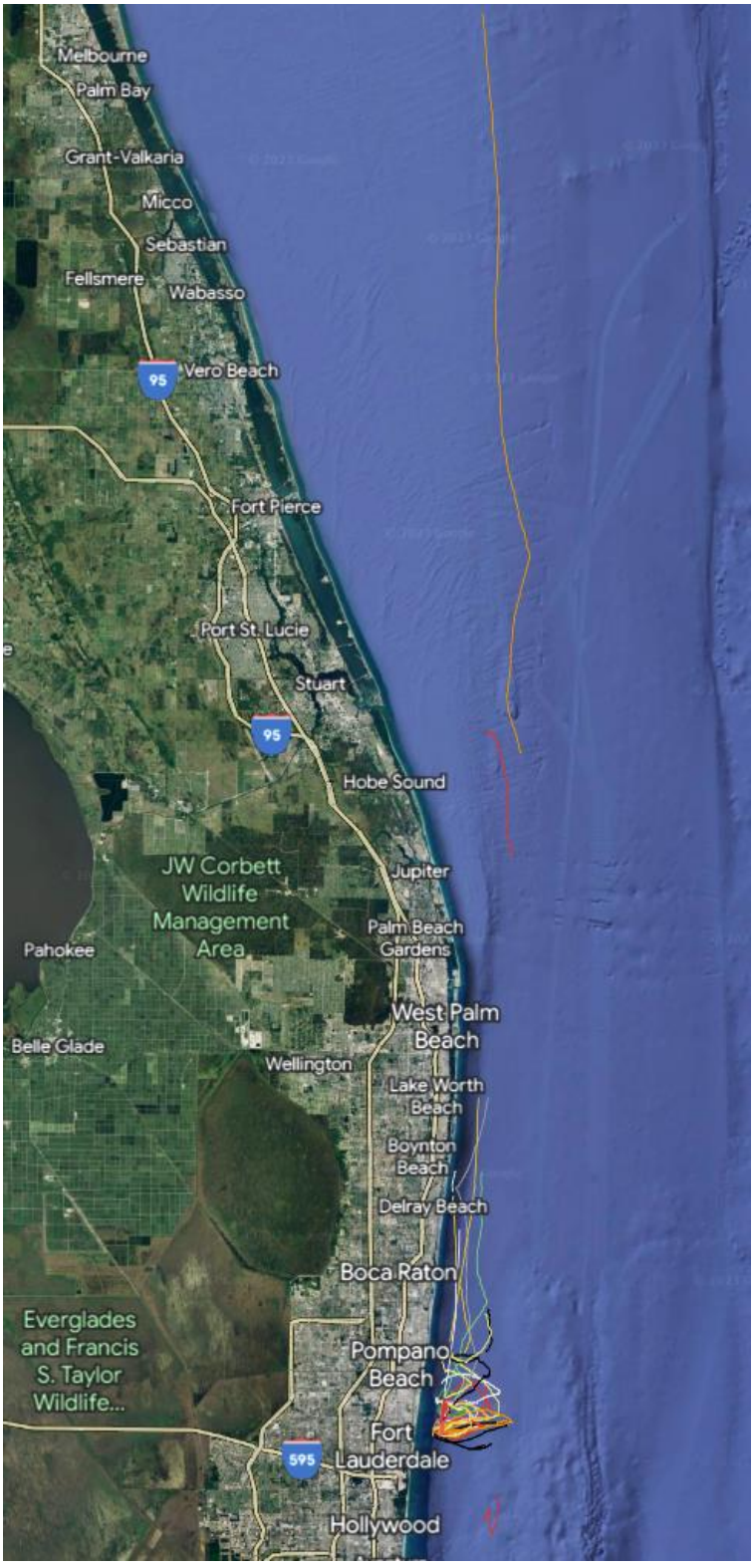

Figure 13. Google Earth view of all the available glider deployment tracks. Deployments began offshore of Fort Lauderdale, 16 km north of the entrance to Port Everglades, Florida, and 8-12 km offshore. Style of track chosen for each deployment varied for either data collection or testing purposes.

Figure 13 shows a Google Earth view with all the deployment tracks that were done for this project. As shown, deployments began and mostly kept in the close vicinity of each other's tracks. All deployments started offshore of Fort Lauderdale, close to Port Everglades, and most were kept within the range limit of Pompano Beach. However, there were a few exceptions, with some continuing all the way north to Stuart, and one even reaching Melbourne. In such cases, the northern flow of the FC was too strong for the glider's propulsion system to overcome and be able to turn around, so the laboratory's crew was forced to travel north for retrieval of the instrument. The style of the track (straight line, circular, zig-zag, etc.) chosen for each deployment was dependent on weather conditions and the purpose of each deployment (data collection or testing purposes). In total, 23 different deployments are available for analysis, most lasting 1 to 2 days and a few lasting up to 3 days. All deployments have available ADCP, CTD, and optics channel data.

For simplicity, it is important to note that all of the color contours that will be shown follow the same structure. This is not restricted to the ADCP measurements, but includes the CTD and optics channel contours as well. Therefore, in the color contours the y-axis represents depth, the x-axis represents time, and the color bar and shading of the figure represents actual measurement values for the variable in consideration. Apart from current direction, all other contours are interpolated between values to smooth the plot for easier visualization. Other example figures that are not shown in the text but were still used for the analysis will be available in the appendices.

Overall results from the velocity contours show the intermittent presence of the SWF varying significantly in strength over time and distance from the shore. The northern component of the SWF was predominantly between -0.1 and -0.3 m/s, sometimes reaching -0.5 m/s, while the northern component of the FC was between 0.5 and 1.4 m/s, sometimes even reaching 2 m/s. Figure 14 provides different examples of deployments that occurred throughout the different seasons of 2022. The contours shown are for current direction and speed in the northern direction. Given that the glider was not measuring at a single location, but rather moving across

and along the shelf, the resulting color contours have a variable seafloor that changes according to where the individual dives took place. The seafloor is represented as a limit by the white background. If the glider was far away from the shore, the water column was deeper and less empty space was visible in the contour (white background), if the glider was close to the shore, the water column was shallower and there was more visible empty space. Therefore, as time advanced it is notable how the seafloor depth also changed as the glider moved towards and away from the coast. Additionally, the glider does not have velocity data for the top two depth bins corresponding to values at 0 m and 5 m due to the ADCP being on the bottom of the instrument and could therefore not record values at those depths. This applies to all available glider deployments.

A)

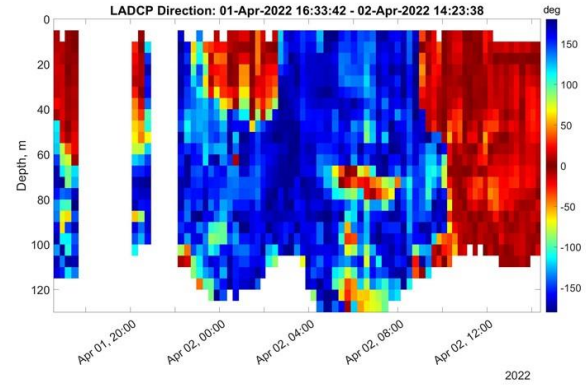
LADCP Direction: 01-Apr-2022 16:33:42 - 02-Apr-2022 14:23:38
deg
Depth, m
Apr 01, 20:00
Apr 02, 00:00
Apr 02, 04:00
Apr 02, 08:00
Apr 02, 12:00
2022

B)

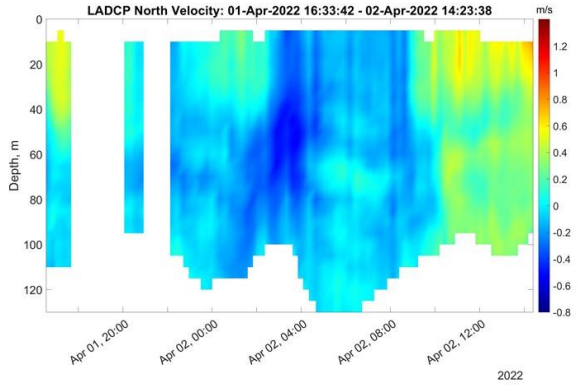
LADCP North Velocity: 01-Apr-2022 16:33:42 - 02-Apr-2022 14:23:38
m/s
Depth, m
Apr 01, 20:00
Apr 02, 00:00
Apr 02, 04:00
Apr 02, 08:00
Apr 02, 12:00
2022

C)

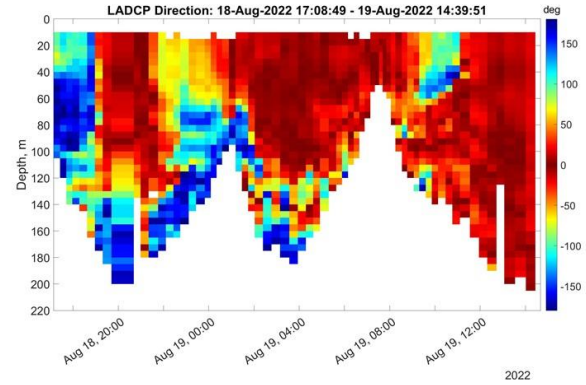
LADCP Direction: 18-Aug-2022 17:08:49 - 19-Aug-2022 14:39:51
deg
Depth, m
Aug 18, 20:00
Aug 19, 00:00
Aug 19, 04:00
Aug 19, 08:00
Aug 19, 12:00
2022

D)

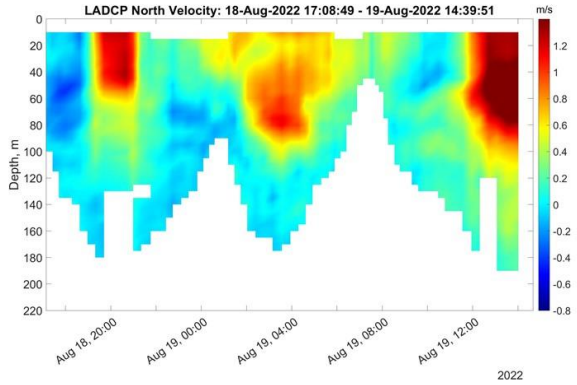
LADCP North Velocity: 18-Aug-2022 17:08:49 - 19-Aug-2022 14:39:51
m/s
Depth, m
Aug 18, 20:00
Aug 19, 00:00
Aug 19, 04:00
Aug 19, 08:00
Aug 19, 12:00
2022

E)

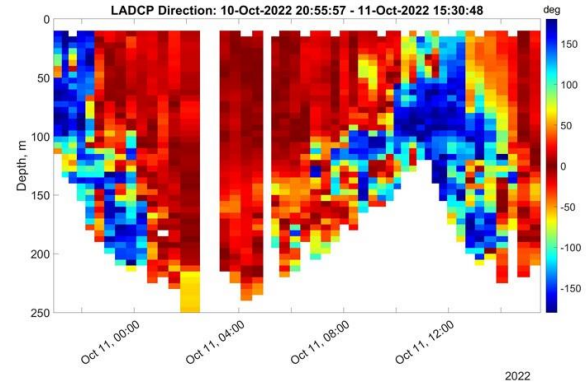
LADCP Direction: 10-Oct-2022 20:55:57 - 11-Oct-2022 15:30:48
deg
Depth, m
Oct 11, 00:00
Oct 11, 04:00
Oct 11, 08:00
Oct 11, 12:00
2022

F)

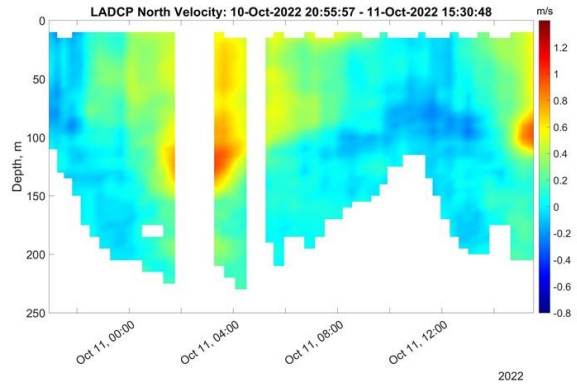
LADCP North Velocity: 10-Oct-2022 20:55:57 - 11-Oct-2022 15:30:48
m/s
Depth, m
Oct 11, 00:00
Oct 11, 04:00
Oct 11, 08:00
Oct 11, 12:00
2022

G)

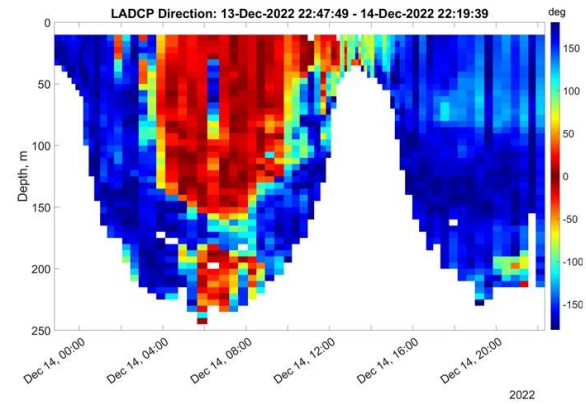
LADCP Direction: 13-Dec-2022 22:47:49 - 14-Dec-2022 22:19:39
deg
Depth, m
Dec 14, 00:00
Dec 14, 04:00
Dec 14, 08:00
Dec 14, 12:00
Dec 14, 16:00
Dec 14, 20:00
2022

H)

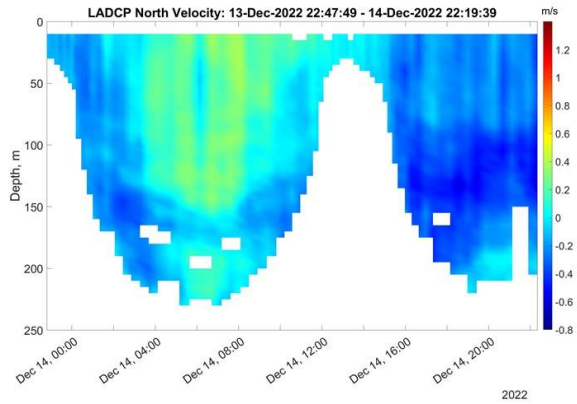
LADCP North Velocity: 13-Dec-2022 22:47:49 - 14-Dec-2022 22:19:39
m/s
Depth, m
Dec 14, 00:00
Dec 14, 04:00
Dec 14, 08:00
Dec 14, 12:00
Dec 14, 16:00
Dec 14, 20:00
2022

Figure 14. Examples of LADCP contours for current direction, left column, and north component of velocity, right column. Current direction was calculated from east and north components of current velocity. Note that depth changes as time advances (white background). This is due to the glider moving across and along the shelf. Shallower depths represent dives when the glider was close to the shore, while deeper depths represent when the glider was offshore. Values of direction go from -180° to 180°, with ±180° being absolute SWF (dark blue), and 0° being absolute northward flow (dark red). Values for northern velocity go from -0.8 m/s (dark blue) to 1.4 m/s (dark red), with 0 m/s represented by a light cyan coloring, with positive values (warmer colors) representing the northward flow and negative values (colder colors) representing the SWF. Each contour pair (i.e. each row) represents a different deployment throughout the 2022 seasons. As such, the 14A and 14B deployment occurred during the spring, the 14C and 14D deployment occurred during the summer, the 14E and 14F deployment occurred during the fall, and the 14G and 14H deployment occurred during the winter.

14A and 14B show a clear appearance of the SWF as a countercurrent, as the blue coloring in the current direction contour spans the entire water column for a significant portion of time. The FC is also visible by the end of the contour. This deployment occurred during the spring season of 2022. 14C and 14D show the SWF as an undercurrent during the first half of the deployment, before disappearing completely during the second half. This was during the summer season of 2022. 14E and 14F show the SWF as both an undercurrent and momentarily as a countercurrent as time advanced. This took place during the fall season of 2022. Finally, 14G and 14H show the SWF as an undercurrent and a dominant countercurrent during a deployment in the winter season of 2022. These 4 cases represent good examples of how the SWF was observed to change throughout the year, but they are not all of the cases taken into consideration. Some examples include deployments when the SWF would be completely absent and only northward flow was observed, deployments when the SWF was observed to be restricted to the coast only, or deployments were the SWF was observed to meander. Additionally, some deployments included corrupted data due to a malfunction of the instruments. That data were not processed alongside the rest so blank zones appear in the contours. For other example LADCP contours from each deployment, please refer to Appendix A.

II. CTD Measurements

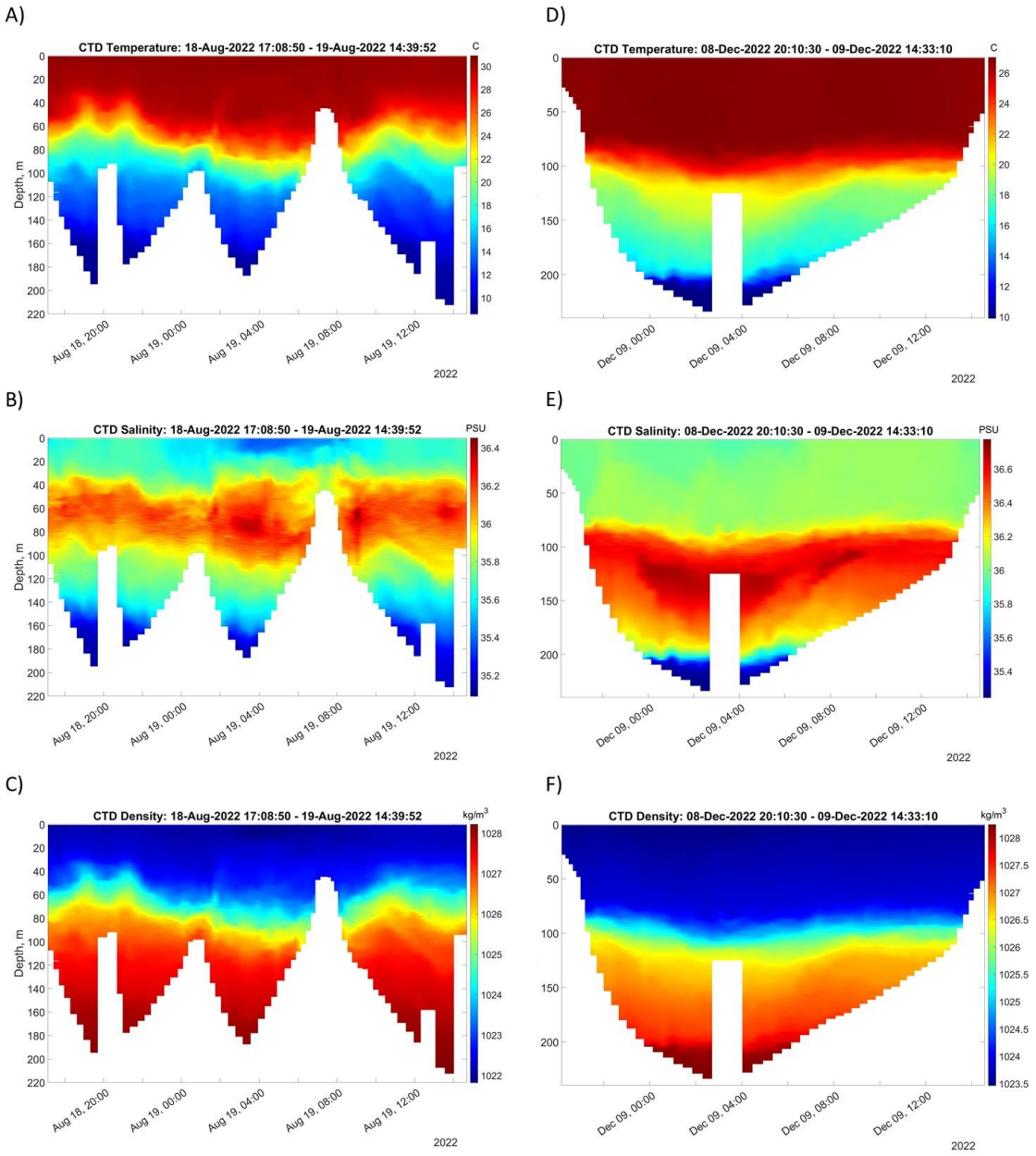

Figure 15. Example CTD color contours for two different deployments. Contours on the left column (15A, 15B, and 15C) correspond to a deployment that occurred during the summer season of 2022. Contours on the right column (15D, 15E, and 15F) correspond to a deployment that occurred during the winter season of 2022.

Figure 15 presents an example of CTD contours from two different deployments that took place during the summer and winter seasons of 2022. The left column represents the contours from a deployment that occurred during the summer season of 2022, and the right column the

contours from a deployment that occurred during the winter season of 2022. Similar to the velocity contours, the depth varied as time went by due to the glider navigating towards and away from the coast during the deployments. Additionally, some CTD contours have some white boxes of missing data. In Figure 15 above this is visible at 20:00 on August 18th, at 13:00 and 14:00 on August 19th, and between 3:00-4:00 on December 9th. These example contours are a good representation of how the contours for each of these parameters look like for all deployments, but they are not necessarily quantitatively similar. To view other example CTD contours for deployments please refer to Appendix B.

Overall, surface waters were around 3-5°C colder during the periods closer to winter, while temperatures in deep waters decreased between 1-2°C. Surface salinities seemed to have slightly increased by about 0.2-0.3 PSU during the winter period when compared against the summer and fall period, and deep water salinities also seemed to have increased by about the same amount. Surface densities increased by 1-2 kg/m^3 during the winter period, while deep water densities remained relatively similar throughout the year. By looking at the temperature and density contours of the deployments, the mixed layer depth seemed to be present at around 60-80 m during the summer and between 100-140 m during the winter. The salinity maximum for most deployments does not occur at the seafloor, but rather at a point halfway to 2/3rds of the way to the seafloor from the sea surface. The data summarizing the CTD results is shown in Table E.1. Table E.1 shows minimum, maximum, and average values of the temperature, salinity, and density measurements at the surface layer (top 20 m) and at the bottom layer (bottom 20 m) of each deployment. Table E.2 shows averages of surface and bottom parameters by season.

III. Intercalibration of Instrumentation

For the available Wirewalker deployment, a comparison between CTD measurements and LADCP calculated components of velocities of the Wirewalker and the glider was done. The comparison was made visually using the contours of Figure 16 and Figure 17, and also statistically by using Pearson correlation coefficients for all available variables. Units for the parameters are the same as the ones specified in the sections above. Note that since the Wirewalker is only moving in the vertical direction, the seafloor does not change significantly as time advances. However, since the glider is moving between two waypoints, the seafloor varies and so the white background is not constant.

Contours from the CTDs of both instruments show an anomaly at the sea surface consisting of a less salty and less dense body of water. Measurements from all three CTD parameters appear to be coherent between both instruments, with similar stratification and strength of color at similar times and places in the water column. Temperature maximum recorded by both instruments is around 28°C at the sea surface, and a minimum of about 15°C near the seafloor. Salinity maximums are around 36.3 PSU at 80 m depths, and a minimum of 35.4 at the sea surface. Density maximum was around 1027 kg/m^3 at the seafloor, and a minimum of about 1022.5 kg/m^3 at the sea surface. The mixed layer depth, estimated from the temperature and density contours, appears to be at a 40 m depth. Measurements of the components of velocity also show good coherence between instruments, after motion correction. The eastern component of velocity is harder to compare due to values being close to 0 throughout the entire deployment, but both instruments still showed similar patterns. The northern component of velocity shows a very similar features from both instruments. Above the 60 m depth layer, the northward flowing FC is evident at a maximum strength of about 0.6 m/s, while below that layer the SWF is present as an undercurrent with a maximum strength of about 0.5 m/s.

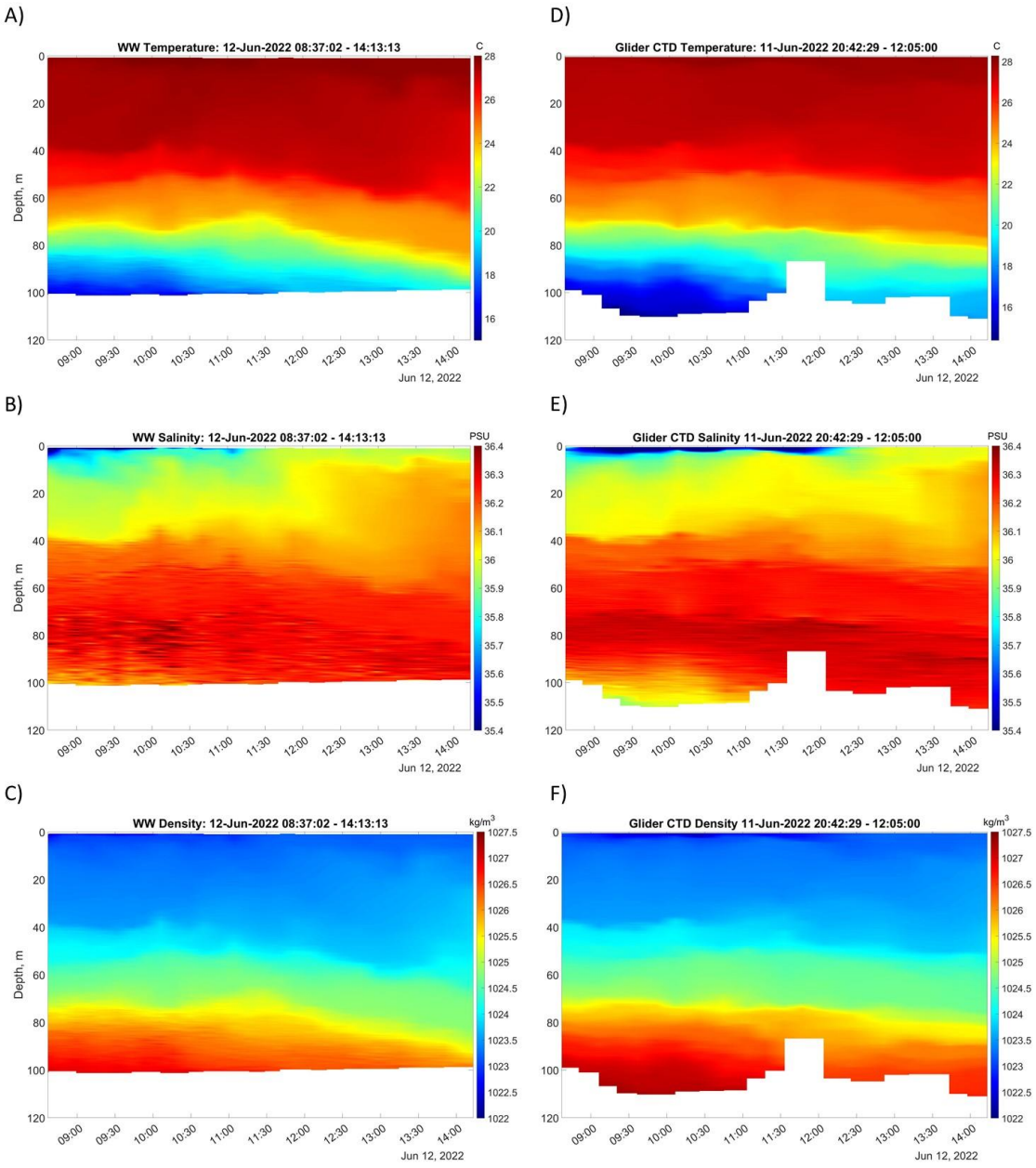

Figure 16. CTD measurement contours. Contours on the left column (16A, 16B, and 16C) are from the Wirewalker, while contours on the right column (16D, 16E, and 16F) are from the glider. The contours are from a deployment where both instruments were in the ocean at the same time and in the vicinity of each other. Note that the seafloor is variable in the glider contours due to navigation of the instrument between two waypoints, while it is relatively constant in the Wirewalker contours due to its movement being restricted to the vertical direction only.

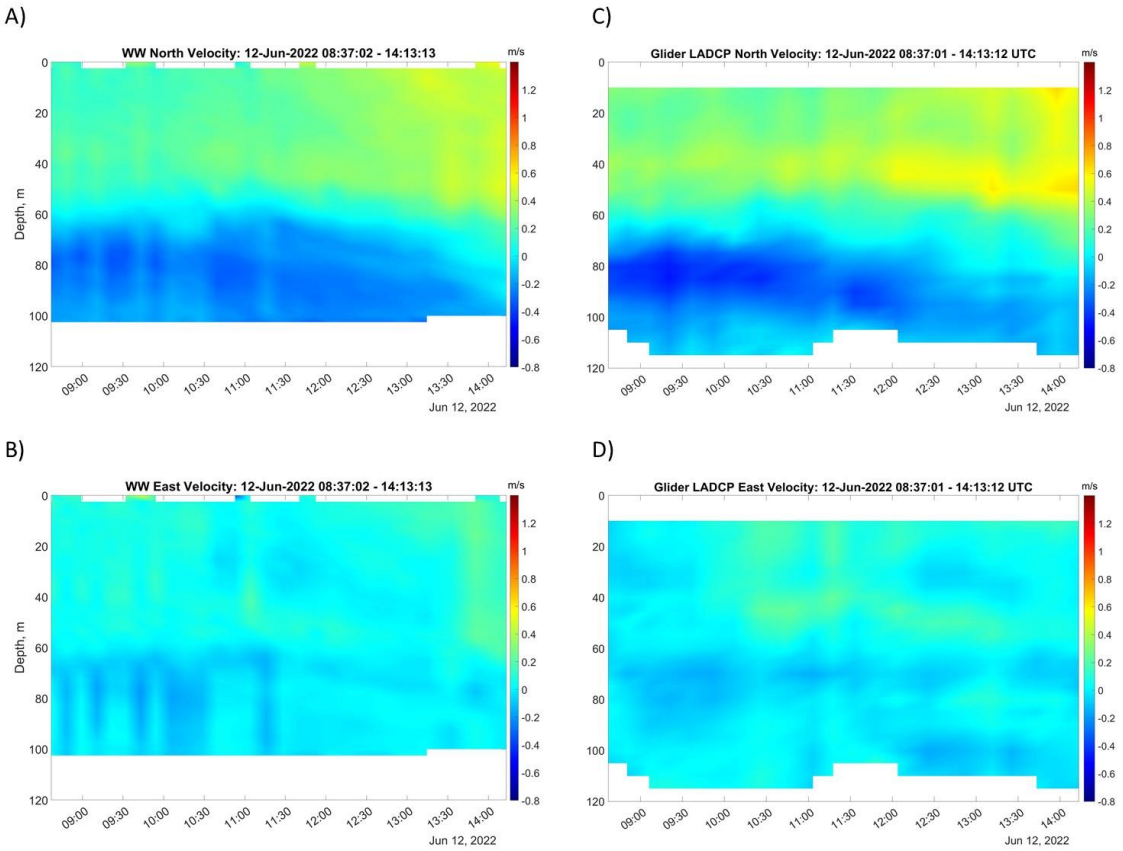

Figure 17. Contours of the components of velocities for the Wirewalker (17A and 17B) and the glider (17C and 17D).

All Pearson correlation coefficients for the comparison between both instruments' CTD measurements and velocity components were significant (i.e. p-values < 0.05). The R values calculated were 0.995 for temperature, 0.873 for salinity, 0.995 for density, 0.953 for velocity north, and 0.410 for velocity east.

IV. Optical Measurements

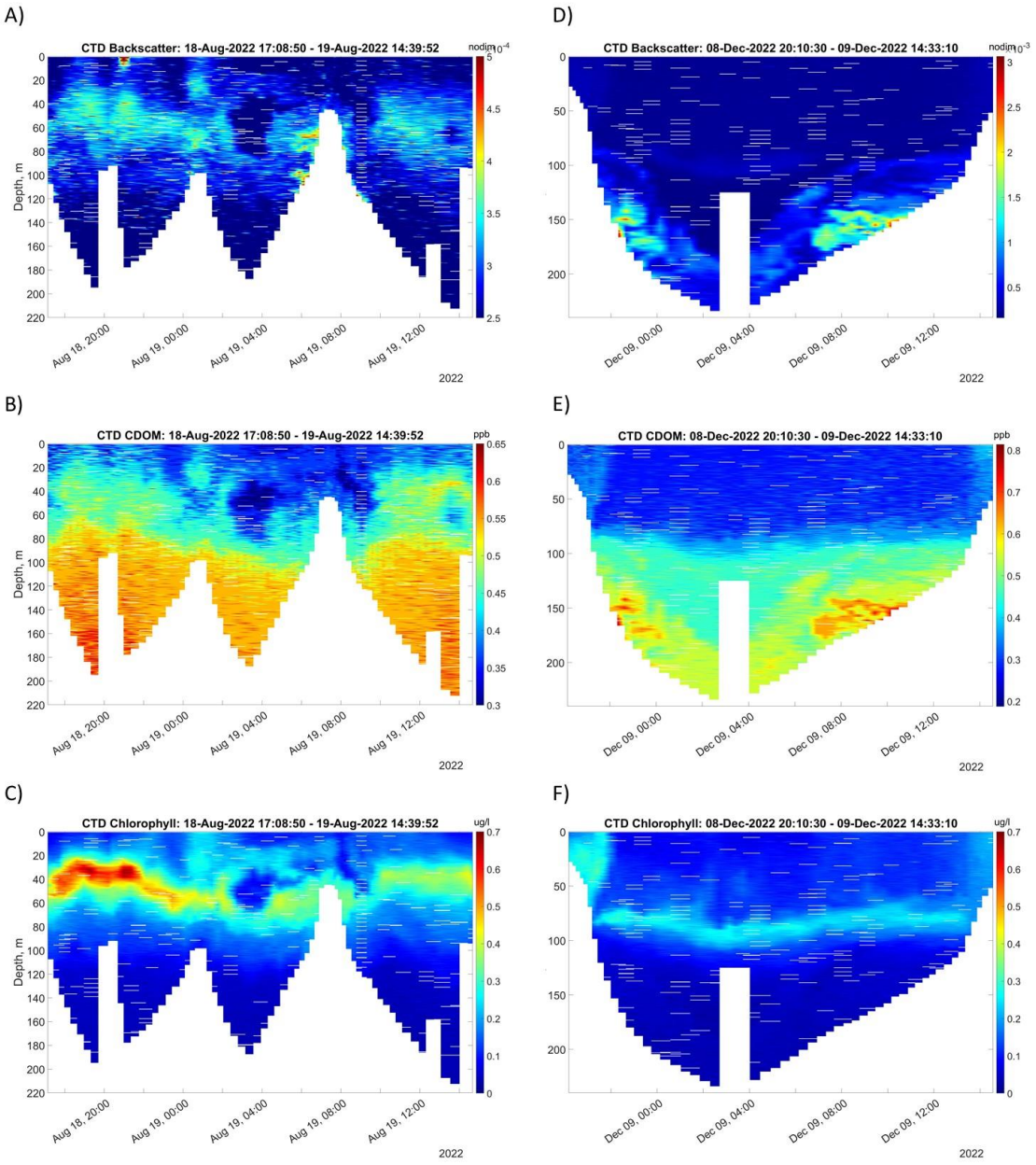

Figure 18. Example optical channels color contours for two different deployments. Contours on the left column (15A, 15B, and 15C) correspond to a deployment that occurred during the summer season of 2022. Contours on the right column (15D, 15E, and 15F) correspond to a deployment that occurred during the winter season of 2022.

Figure 18 presents an example of the optical contours from two different deployments that took place during the summer and winter seasons of 2022. These are the same two example deployments seen in Figure 15. The left column represents the contours from a deployment that

occurred during the summer season of 2022, and the right column the contours from a deployment that occurred during the winter season of 2022. As observed in the CTD contours, the depth varied as time went by due to the glider navigating towards and away from the coast during the deployments. Again, and similarly to the CTD contours, there's some white boxes of either missing data or outside interference that prevented the glider from moving further down the water column. These example contours are a good representation of how the contours for each of these parameters look like for all deployments, but they are not necessarily quantitatively similar. To view other example optical channel contours please refer to Appendix C.

Overall, surface backscatter seemed to have decreased slightly as winter approached, while backscatter near the seafloor seemed to have increased slightly. Surface CDOM decreased by about 0.1 ppb during the winter, and then by about 0.2 ppb during the spring, while bottom CDOM seemed to have decreased by 0.05 ppb during the winter, and then decreased by 0.25 ppb during the spring. Surface chlorophyll levels decreased by about 0.2 μg/L during the winter, and quickly increased by 0.1 μg/L during the spring, while bottom chlorophyll levels decreased by 0.05 μg/L during the winter, and increased by 0.05 μg/L during the spring. Important considerations to have include that surface backscatter might be high due to surface reflections or noise from the sea surface and chlorophyll maximums were usually not located at the sea surface, but at around 30-50 m depths. The data summarizing the optical channels results is shown in Table E.3. Table E.3 shows minimum, maximum, and average values of the backscatter, CDOM, and chlorophyll measurements at the surface layer (top 20 m) and at the bottom layer (bottom 20 m) of each deployment. Table E.4 shows averages of surface and bottom parameters by season.

V. 3D Figures and Eddies

The 3D plots of north velocity are a representation of the 2D contours on 3D space to easily visualize changes in current magnitude and direction as time went by and the glider moved towards and away from the coast. Figure 19 shows three example plots for when the SWF was absent, present as an undercurrent, and present as both an undercurrent and a countercurrent. Most of the contours include vectors of current direction for the 20 m depth bin. The 3 contours in Figure 19 are shown as examples of how different variations of the plots may appear, but they are not all necessarily similar, nor are they the only ones taken into consideration for analysis. Other 3D figures include variations in the glider tracking/pathing across and along the shelf, varying strengths of current velocities, and latitude ranges. To look at other example 3D figures please refer to the Appendix A.

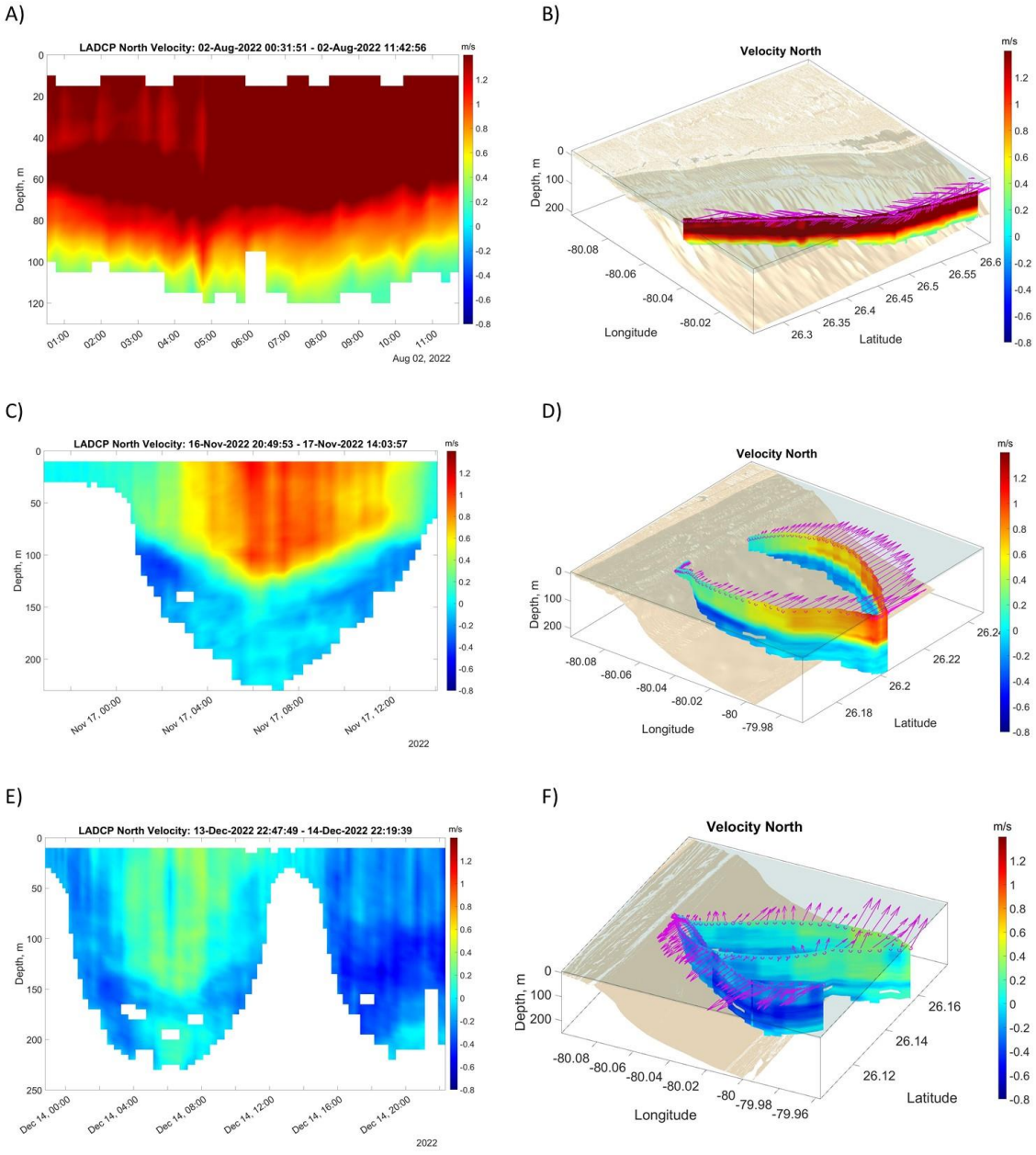

Figure 19. Examples of different 3D plots. Contours 19A and 19B correspond to a deployment that occurred during the summer of 2022 and the SWF was missing. Contours 19C and 19D correspond to a deployment that occurred during fall of 2022 and the SWF was present as an undercurrent. Contours 19E and 19F correspond to a deployment that occurred during the winter of 2022 and the SWF was present as an undercurrent at first, and then as a countercurrent. The plots on the right column are the same as the contours on the left column, but plotted with glider tracking as well to facilitate the visualization of movement across and along the shelf. Local bottom topography is also included. Vectors in these plots are for the 20 m depth bin.

For some of the deployments whenever the SWF was present, the vector plots revealed the appearance of eddy-like features in the form of a counterclockwise rotation of the vectors, as shown in the example in Figure 20. This rotation seemed to be restricted to the continental slope, and appeared only close to the coast. The rotation of the vectors was only visible whenever the SWF was present, but it was not restricted to its appearance as either an undercurrent or a countercurrent.

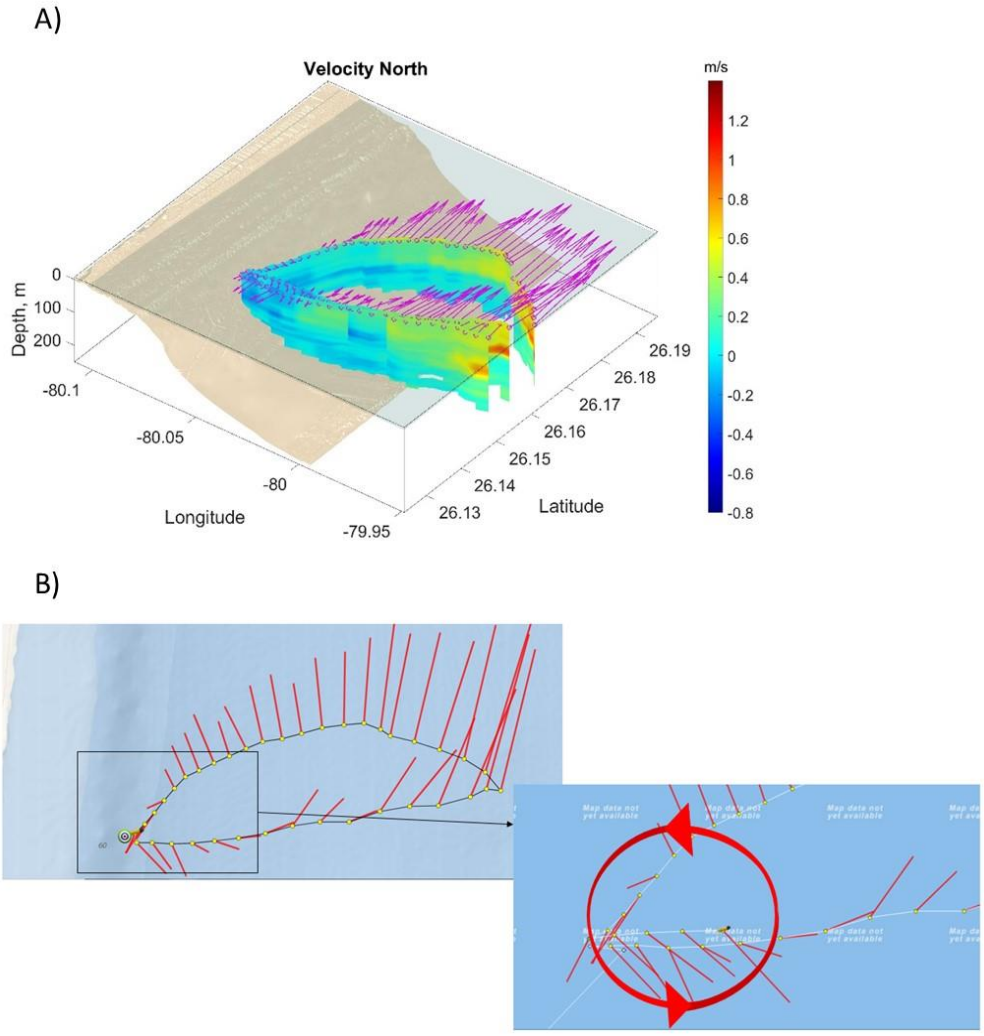

Figure 20. Velocity contour for the northern component of the current throughout time and depth and a vector plot showing overall current direction. Vectors provided for the 20 m depth bin. Contour is for glider deployment that occurred on 10-11 October 2022. 20B is a graphic highlighting the eddy-like feature observed from the vector plot in 20A.

VI. Turbulence

Results from the Richardson number contours were inconclusive at best. For all deployments, the Richardson number (Ri) was calculated at every available depth bin and their arctangent was plotted. The arctangent was plotted to keep the Ri below 1.6. The Richardson number color contours used for analysis were modified so that only critical values were plotted. The critical value chosen was 0.3, and as such only depth bins were the Ri was below 0.3 are visible, as seen in Figure 21. The figure shows the three same example deployments used in Figure 19. These are shown as examples of how different variations of the plots may appear, but they are not all necessarily similar, nor are they the only ones taken into consideration for analysis. To look at other example Richardson number contours please refer to the Appendix D.

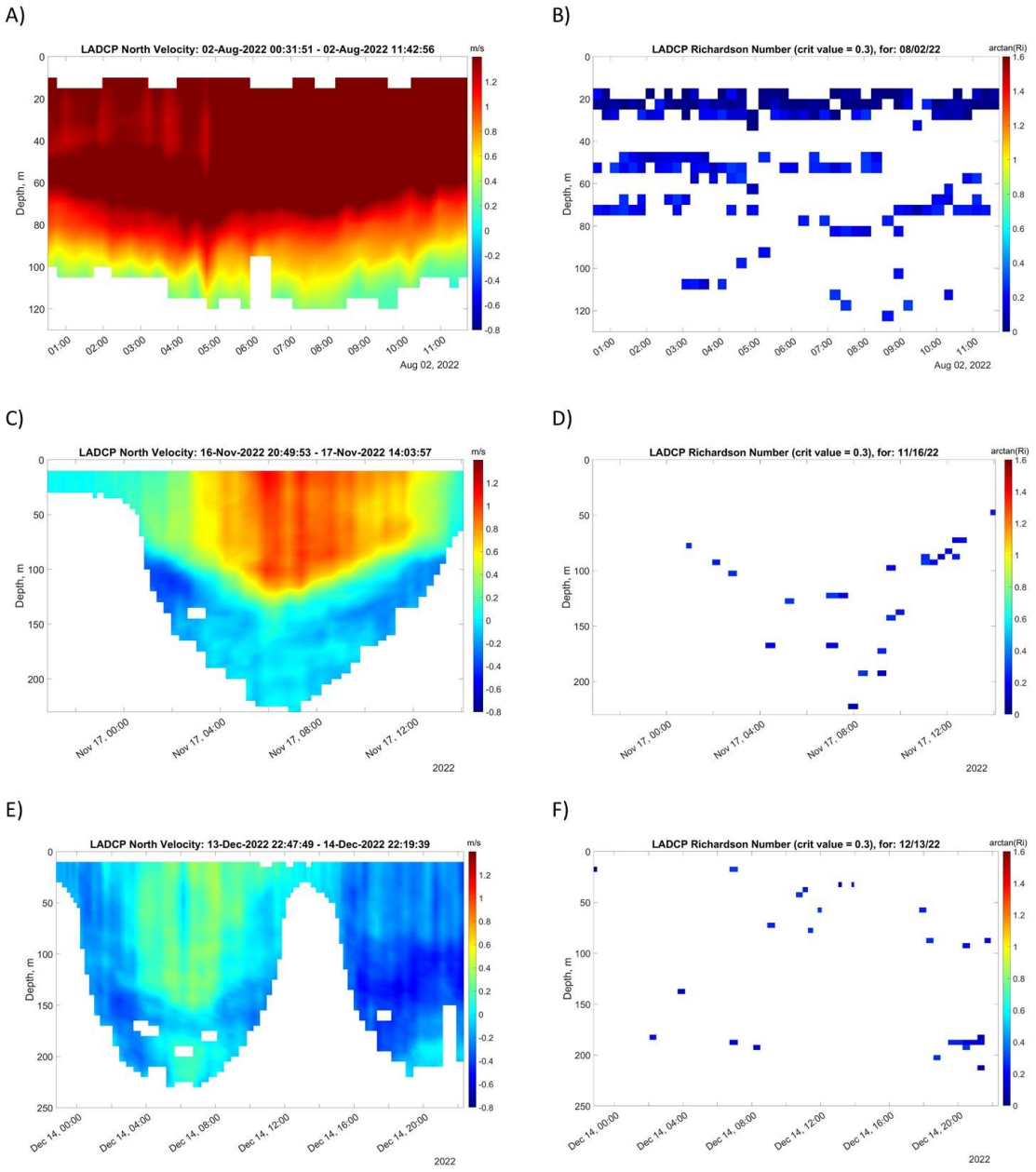

Figure 21. Example of Richardson number contours from the 3 deployments presented in Figure 19. Contours 19A and 19B correspond to a deployment that occurred during the summer of 2022 and the SWF was missing. Contours 19C and 19D correspond to a deployment that occurred during fall of 2022 and the SWF was present as an undercurrent. Contours 19E and 19F correspond to a deployment that occurred during the winter of 2022 and the SWF was present as an undercurrent at first, and then as a countercurrent. The contours on the right only portray Richardson numbers that were below the critical value of 0.3 to easily visualize where critical values were reached and overturning of the water column occurred.

Overall, Richardson numbers were expected to reach critical values at three places: the sea surface, the near-bottom layer, and the interface between the northward flowing FC and the SWF. However, no visible pattern was consistent across all deployments. Critical values at the sea surface were observed in most cases when the FC or the SWF reached high velocities, but that was not always true. Critical values near the seafloor were also observed in similar situations, but were much scarcer than at the sea surface. Critical values at the interface happened for some deployments, but not for others, and no relationship with current velocities was discernible. Finally, for all deployments there were also a scarce scattering of seemingly random critical values at various depth bins, and no relationship was visible between them and the velocity field.

VII. Upwelling

Analysis of velocities, temperature, depth, colored dissolved organic matter (CDOM), and chlorophyll occurred in the form of visual assessment and correlation analysis with the northern velocity. Pearson correlation coefficients were obtained for 5 distinct scenarios: all deployments, deployments where the southward flow was absent, all when it was present, when it showed as an undercurrent, and when it showed as a countercurrent. Table 1 shows the correlation coefficients, R, and their p-values for a 95% confidence test for all of these comparisons.

Table 1. Correlation analysis results for the detection of possible upwelling. 5 different scenarios are taken into consideration and color coded: data from all deployments (blue), data from deployments where the southward flow was minimal or completely absent (green), data from deployments where the southward flow was prominent as either an undercurrent or a countercurrent (orange), data from deployments where the southward flow appeared as an undercurrent (red), and data from deployments where the southward flow appeared as a countercurrent (purple). Variable 1 is represented by north velocity in all 5 different scenarios, variable 2 is each different variable it was tested against for all 5 different scenarios.

Variable 1	**Variable 2**	**Correlation Coefficient (R)**	**p-value**
North Velocity (all)	Temperature (all)	0.44	< 0.01
North Velocity (all)	East Velocity (all)	0.32	< 0.01
North Velocity (all)	Depth (all)	-0.39	< 0.01
North Velocity (all)	CDOM (all)	-0.16	< 0.01
North Velocity (all)	Chlorophyll (all)	0.29	< 0.01

North Velocity (South flow minimal/absent)	Temperature (South flow minimal/absent)	0.49	< 0.01
North Velocity (South flow minimal/absent)	East Velocity (South flow minimal/absent)	0.15	< 0.01
North Velocity (South flow minimal/absent)	Depth (South flow minimal/absent)	-0.40	< 0.01
North Velocity (South flow minimal/absent)	CDOM (South flow minimal/absent)	-0.06	< 0.01
North Velocity (South flow minimal/absent)	Chlorophyll (South flow minimal/absent)	0.11	< 0.01
North Velocity (South flow present)	Temperature (South flow present)	0.42	< 0.01
North Velocity (South flow present)	East Velocity (South flow present)	0.36	< 0.01
North Velocity (South flow present)	Depth (South flow present)	-0.38	< 0.01
North Velocity (South flow present)	CDOM (South flow present)	-0.16	< 0.01
North Velocity (South flow present)	Chlorophyll (South flow present)	0.29	< 0.01
North Velocity (South flow as undercurrent)	Temperature (South flow as undercurrent)	0.55	< 0.01
North Velocity (South flow as undercurrent)	East Velocity (South flow as undercurrent)	0.43	< 0.01
North Velocity (South flow as undercurrent)	Depth (South flow as undercurrent)	-0.42	< 0.01
North Velocity (South flow as undercurrent)	CDOM (South flow as undercurrent)	-0.03	< 0.01
North Velocity (South flow as undercurrent)	Chlorophyll (South flow as undercurrent)	0.33	< 0.01
North Velocity (South flow as countercurrent)	Temperature (South flow as countercurrent)	0.35	< 0.01
North Velocity (South flow as countercurrent)	East Velocity (South flow as countercurrent)	0.29	< 0.01
North Velocity (South flow as countercurrent)	Depth (South flow as countercurrent)	-0.36	< 0.01

North Velocity (South flow as countercurrent)	CDOM (South flow as countercurrent)	-0.25	< 0.01
North Velocity (South flow as countercurrent)	Chlorophyll (South flow as countercurrent)	0.31	< 0.01

7. Discussion

I. Intercalibration of Instruments

Wirewalker and glider contours compare fairly well qualitatively. Water masses in the ocean are bodies of water that can be identified by a distinctive combination of temperature, salinity, and density ranges caused by localized climatic effects (Brittanica, 2015). In the case of this intercalibration, it was observed that the CTD contours of both instruments show incredible coherence across the entire water column. This shows that they are indeed measuring the same water mass, and allows for a comparison between velocity measurements. To further validate these results, the R coefficients from the correlation analysis are also taken into consideration. For all 3 CTD measurements, R values of above 0.8 were obtained, with p-values below the significance level of 0.05. Therefore, it can be stated that temperature, salinity, and density measurements from the glider are significantly strongly positively correlated to the temperature, salinity, and density measurements from the Wirewalker, respectively.

In the case of the eastern and northern velocity, the contours compare fairly well qualitatively. However, while the northern component shows great coherence, the eastern velocity is harder to discern. R coefficients for the velocity north and velocity east are 0.953 and 0.410, respectively, with p-values lower than the significance level of 0.05. Therefore, it can be stated that northern velocity measurements from the glider are significantly strongly positively correlated to the northern velocity measurements from the Wirewalker. It can also be stated that eastern velocity measurements from the glider are significantly moderately positively correlated to the eastern velocity measurements from the Wirewalker.

An interesting feature tying the CTD and the velocity contours together is the presence of the mixed layer depth. As mentioned before, the presence of the SWF in its different forms is dependent on the seasonally varying strength of water column stratification. Surface temperature were observed to reach close to 28°C, while bottom temperatures remained at around 15°C. From the CTD contours, the mixed layer depth seems to be present at around the 40-60 m depth.

From the velocity contours, it is also visible that the SWF, as an undercurrent, is restricted to below the 60 m depth layer. This is most likely a cause of a strong temperature stratification, which restricts the SWF appearance to the depths.

From the CTD contours, the only unexpected feature is the sea surface anomaly mentioned during the results. Due to the location of the instruments' deployment, it is fair to assume that this surface anomaly is a results from coastal outflow coming from the nearby Port Everglades. Although not a certainty, this assumption seems to be a fair observation since the sea surface anomaly was also present during other glider deployments in the area. Figure 22 below shows the glider's CTD and optical channels contours for the deployment used during the Wirewalker comparison side by side. When looking at the time period where the sea surface anomaly was observed, it is also clear how the optical channels reflect it as well. During those times, a drastic increase in backscatter, CDOM, and chlorophyll concentrations was observed. Therefore, the presence of this anomaly likely has implications for the transportation of pollutants, particulates, and biological material.

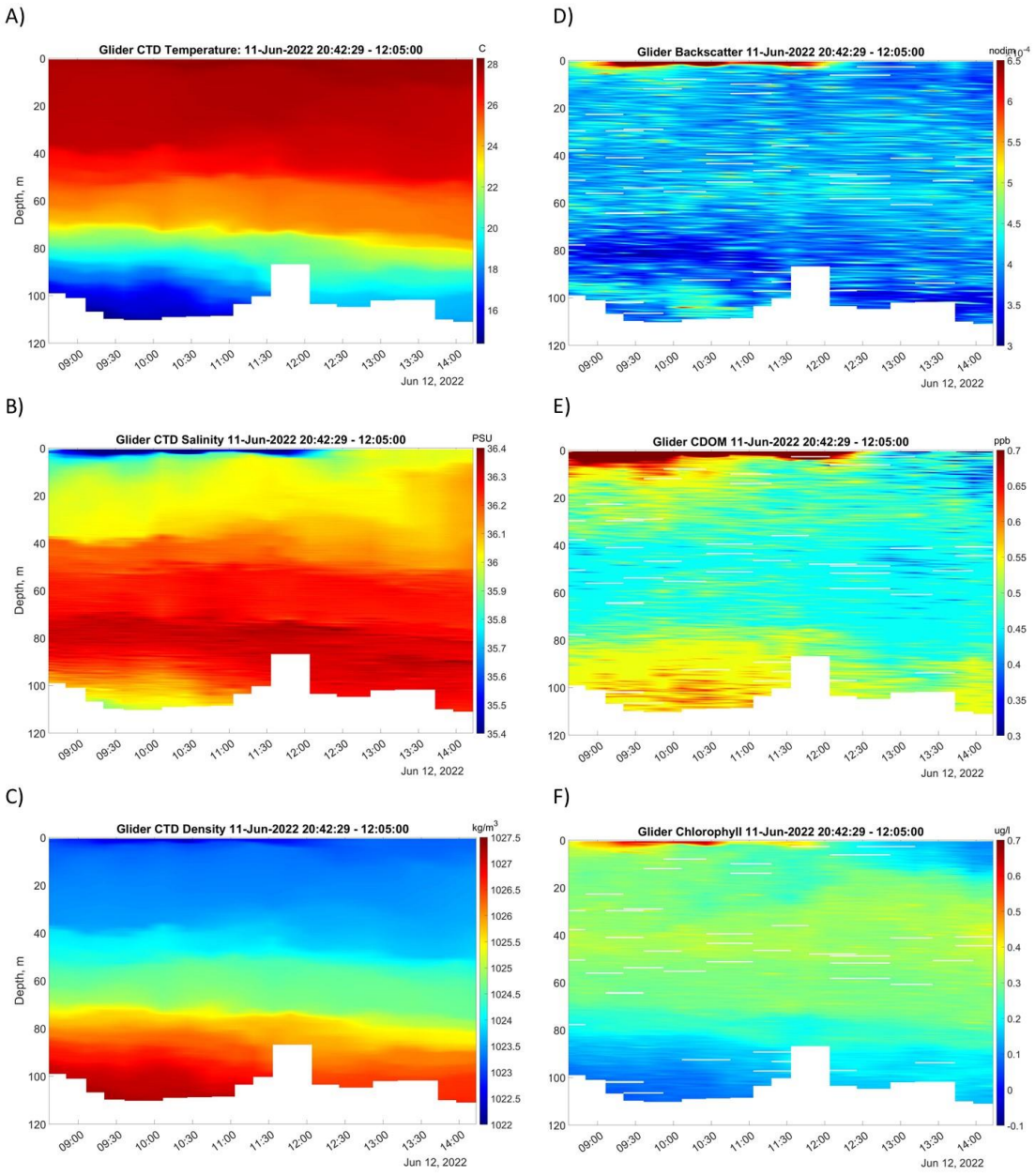

Figure 22. CTD and optical channels contours from the glider for the deployment used during the Wirewalker intercalibration.

II. General Observations of the SWF

Across all deployments, the northern velocity contours and the contours of velocity direction clearly show the presence of an intermittent SWF whose characteristics evolve with both time and space. The SWF was also observed in the 3 distinct forms previously described by Soloviev et al. (2017): as a seasonally dependent countercurrent, as an undercurrent attached to the

continental slope, and as an intermittent undercurrent on the Miami Terrace. We expected that the forms the SWF takes to be dependent on the strength of water column stratification. This could be due to the seasonal variability of strength of the water column stratification. During the summertime strong stratification would prevent the jet from surfacing (keeping it as an undercurrent), while during the wintertime the stratification weakens, and the jet can make it to the surface (as a countercurrent). In our observations, while it is true that the countercurrent appeared more frequently during the winter and spring seasons, it was not necessarily restricted to those only, as it made some appearances during the summer and fall seasons as well. This was also true for the undercurrent, as it also appeared during the winter and spring seasons but was more frequent during the summer and fall. In addition to seasonal variability, the SWF can also be affected by ocean eddies, tides, local climatic conditions, and the meandering of the FC, so multiple factors could have influenced the form the SWF takes.

During the June-September deployments of 2022, the glider track was primarily of the snake-like and straight-line types. Appearance of the SWF was highly time-dependent, since during this period it was not present in some deployments, and in others it seemed to meander within just a few hours. This could probably be due to an appearance of an eddy and perhaps other factors such as internal tides or the meandering of the FC (Soloviev et al, 2003). Additionally, the glider deployments provide only a snapshot-like window view of actual ocean processes, so processes occurring on longer timescales, which could affect the SWF, are not analyzable with the data at hand. The SWF was also more prominent as distance from the shore decreased. This is likely due to the influence of the FC, as its influence and strength seemed to increase with increasing distance from the shore, preventing the formation of the undercurrent. During this summer and early fall period, the undercurrent and intermittent undercurrent forms were the most observed forms of the SWF. In a few deployments the SWF was completely missing, suggesting either a meandering out from the continental slope or a complete lack of it.

During the October-December deployments of 2022, the glider track was kept as a loop to find changes in the SWF through time at the same locations. During this period, the SWF behaved mostly as a countercurrent, but made appearances as an intermittent undercurrent. Like the June-September period, the SWF's presence was mostly seen closer to the shore. Only during the second December deployment, December 13-14, was the countercurrent present further from

the shore. Even then, it was only present during part of the deployment since the loop track had shown northward flow just a few hours before in the vicinity. This, again, could indicate influences from the meandering of the FC, or a meandering of the SWF itself.

During the January-September deployments of 2023, the glider track was primarily of the straight and loop types. This was done to both investigate its behavior further north and analyze changes through time and space at the same locations. During this period, several issues with the glider's ADCP prevented some of the deployments to provide full contours. Both the January and February deployments were incomplete, and the SWF was only observed briefly as a countercurrent close to the coastline. The second March deployment and the June deployments showed the SWF as both a countercurrent close to the shore, and as an undercurrent as the glider moved away from the shore. The August and September deployments were incomplete, but the SWF was observed as an undercurrent only.

Overall, deployment contours show the intermittent presence of the SWF varying significantly in strength over time and distance from the shore. Deployments occurred in the close vicinity of each other's tracks, and variations in contours show the meandering behavior of the SWF into and out of the continental slope. This meandering occurred in the order of a few hours. Additionally, although no quantitative analysis has been done on the subject, qualitative analysis of the contours revealed that the strength of the FC seemed to affect the strength of the SWF, with increasing northward flow slowing down the SWF. The undercurrent form of the SWF appeared more prominently during the warmer months, but also appeared in some deployments during the colder months. Similarly, the countercurrent form of the SWF appeared more prominently during the colder months, but also appeared in some deployments during the warmer months. Local climatic variability is the most likely contributor to these anomalies, but other factors such as long-term oceanic variability, presence of mesoscale eddies, tidal variability, etc., could have contributed as well. Finally, appearance of the SWF as a countercurrent was mostly observed close to the shore, while appearance of the SWF as an undercurrent was observed as distance from the shore increased. This is most likely due to the influence of the FC, as it dominated offshore, and the Coriolis force, as it would push the undercurrent at depth towards the shore until it rose as a countercurrent.

III. Temperature, Salinity, and Density

As expected, surface temperatures decreased during the colder months while temperatures in deep waters decreased by a smaller amount. The difference in the range of temperatures between the colder and warmer months is most likely a primary driving force for the form the SWF may take. When observed as an undercurrent, the SWF would be restricted to the depths below the mixed layer depth observed from the pycnocline. This was observed primarily during the summer months as sea surface temperatures were at a highest and stratification was at its strongest. As stratification strength decreases due to a smaller temperature range in the winter, the SWF is then able to move past the mixed layer depth and appear as a countercurrent spanning the entire water column. Similarly, and as expected, since water is denser as temperatures decrease the mixed layer depth also saw a deepening during the winter. Sea surface salinities slightly increased during the winter period, most likely due to the later summer period being a part of the local rainy season. However, it's important to note that surface salinity increases due to lower amounts of rain is hard to understand.

A trend appears after looking at all three contours of density, temperature, and salinity together. As expected, density increases and temperature decreases with increasing depth. Salinity, however, increases to a maximum at around halfway through the water column, before decreasing to a minimum close to the seafloor, in almost all the deployments. With this type of structure in salinity by itself, it would be expected that the water column would overturn due to instability, but the density contour shows a stable gradient throughout. This can be explained by the stabilizing effect of the temperature stratification. This temperature difference at the point of maximum salinity vs the point of minimum salinity in the same ensemble is almost constantly about 10-12°C, which could help explain how lower salinity, but colder water stays below the higher salinity but warmer water. This kind of feature is known to be common for coastal oceans, and no relationship between this salinity inversion and the SWF was found.

A significant amount of deployments also showed the sea surface anomaly previously discussed during section I of the discussion. As mentioned before, this anomaly is most likely caused by the outflow of fresher waters from Port Everglades, which was near the glider's deployment site. Nevertheless, this is hard to observe exclusively from CTD measurements, so the optical channels measurements are also taken into consideration in the section below.

IV. Transport of Particulates and Biological Material

Backscatter counts seemed to peak at 3 different locations, varying by deployment: at the seafloor, at the layer of maximum chlorophyll concentrations, and at the sea surface. Both close to the seafloor and at the layer of maximum chlorophyll concentrations backscatter counts behaved as expected. Peaks close to the seafloor are likely caused by increased concentrations of particulate matter, sediment uplifting by benthic organisms, or could even be noise from reflections from the seafloor. Peaks at the layer of maximum chlorophyll are likely caused by the primary producing organisms and detritus from trophic interactions. Peaks at the sea surface are intermittent, but coincide for the most part with the sea surface anomaly observed from the CTD contours. It can therefore be said that Port Everglades is outflowing a significant amount of particulates onto coastal waters. This could have important implications as these particulates are not restricted to only biological material, but could also include, for example, pollutants. Another type of peak observed occurs when the glider was closer to the coast. Theoretically, mixing would be more intense at shallower depths, and so more sediment or particulates would be present in the water column which would drive backscatter counts up. This was expected and observed, however, no saturation conditions or measurements are available at this time. No relationship between the SWF and backscatter counts was observed.

CDOM concentrations peaked at two different locations: at the seafloor and at the sea surface. It is important to note that CDOM concentrations were not restricted to the area just above the seafloor, but they were observed to extend up to 60-80 m above it. For this reason, there seemed to be a negligible to no strength of association between the SWF and CDOM concentrations. Although not observed exclusively in the depths that the undercurrent operates, CDOM concentrations do peak in that area and the depths above. Therefore, at least to some minor degree, CDOM is being transported southwards. How meaningful, large, and different this movement of CDOM is compared to the movement of CDOM by the FC cannot be currently understood, but should be investigated further. Similar to backscatter counts, CDOM concentrations also peaked when the glider was closer to the coast, which makes sense since waters close to the shore are typically very productive. Finally, CDOM concentrations also peaked at the sea surface at times when the anomaly previously mentioned was observed. These observations led us to conclude that Port Everglades is also outflowing a significant amount of

biological material, which could have severe implications for biological activity, and could even alter trophic interactions.

Chlorophyll concentrations were observed to peak at two different locations: at a depth layer between 40-60 m depending on the deployment and at the sea surface. This 40-60 m depth layer of peak chlorophyll concentrations was observed to closely follow the depth of the start of the pycnocline across all deployments. As expected, a medium positive strength of association was observed between chlorophyll and the northern flow. Even as a countercurrent, it doesn't seem that the SWF affects chlorophyll concentrations in any significant way. At the sea surface, chlorophyll concentrations were also observed to peak at deployments and times when the sea surface anomaly was observed. Therefore, the outflow from Port Everglades is either moving a significant amount of primary producers to the coastal ocean, or the nutrients, particulates, and biological material it is outflowing are directly affecting and increasing primary productivity. If unchecked, this type of sudden increase in productivity could lead to detrimental conditions, such as the sudden appearance of diatom blooms, hypoxic conditions, etc.

Overall, it was observed that to a minor degree the SWF might be transporting particulates and biological material. This does not mean they originate from the SWF rather that they are coming from a source further north and are being transported southwards. With the available data so far, it is not possible how this transport could affect biological activity further south, more research is needed in this aspect. The SWF also did not seem to affect the transport of primary producers. This is most likely due to the depth layer at which primary producers were observed to peak at, which lies just above the pycnocline. Differences in this depth layer appeared to be unaffected by whether the SWF or the FC dominated, so there was no significant relationship observed between the SWF and chlorophyll concentrations. Finally, the outflow of fresher water from Port Everglades appears to be a significant source of particulates and biological material, which likely drives increased primary productivity at the surface layer. At this time, the beneficial or detrimental effects it might be having have not yet been studied. Nevertheless, both the SWF and the FC have been observed to actively transport this water, so the reach and potential to alter local trophic interactions is likely larger than previously thought.

V. Eddy Activity

As shown in Figure 20, some deployments' vector plots showed a counterclockwise rotation of the vectors. These patterns are likely due to eddy features appearing either to modify the SWF or in response to it. When the SWF is present, eddy features seem to appear close to the shore, rotating in a counterclockwise, cyclonic direction. Previous research in the California Current showed that eddy-like features are able to disrupt coastal flow of an undercurrent (Hickey, 1998). On the other hand, there has been evidence of eddy formation off the coast of south-west Australia due to the interactions between overlying currents, undercurrents, and bottom topography (Rennie et al., 2007). In the 3D plots, the rotational motion of the velocity vectors as the deployments went by is considered to be an "eddy-like" feature. While the SWF resulted in purely southwards motion of the water, these eddy-like features also showed motion not only along the coast, but also across. As such, the SWF was observed to be dominant offshore, while eddy-like features were only observed close to the coastline. However, in the FC, whether eddies are naturally occurring and coincide with the SWF or if they appear as a response to the SWF is still unknown. Nevertheless, our data seems to support that the SWF and coastal ocean eddies are part of a coupled system. Similar systems have been previously shown to exist for shallow undercurrents in the continental shelf of western boundary currents, such as in the Bay of Bengal and the Philippines (Francis et al., 2020; Qu et al., 2012). The eddy-like features were not observed offshore or when the SWF was absent. Additionally, the rotational motion of the vectors appeared to appear or disappear in deployments where the glider passed through the same place more than once. This suggests that the eddy-features are likely moving along the coast, most likely southwards, but concrete evidence for the direction of their movement has not been found yet.

VI. Turbulent Flow

The Richardson number serves to indicate dynamically unstable shear conditions in a stratified water column. Richardson numbers below the theoretical critical value, 0.25, point towards unstable conditions and generally result in turbulent mixing. The critical value of 0.25 is the one generally used in scientific research, but it may vary in between 0.2 and 1.0 depending on experimental or natural conditions (Galperin et al., 2007). Here, a critical value of 0.3 was chosen after using a 0.25 value proved to be insufficient. The Richardson number generally

shows below critical values at the sea surface, along the transitional layer between the SWF and the overlying FC, and near the bottom. However, our results also proved to not be consistent throughout all of the deployments. Critical values were reached at the sea surface for almost all deployments, which is to be expected given how volatile the sea surface is. At the interface layer between the SWF and the FC some deployments showed critical values, others didn't. We expected to see much more turbulent flow at this layer, since the differences between the two oppositely driven bodies of water and bottom friction should affect turbulence in the transition and near the bottom layer. However, this was not the observed case. A possible explanation is that 0.3 might still be too low of a critical value to observe this turbulent mixing, so more research is needed. Additionally, increasing the critical value might prove to be detrimental, since an increase from 0.25 to 0.3 already increased the number of critical value observations in the surface layer significantly, as well as in seemingly random parts of the water column. Increasing the critical value might then result in much more noise than meaningful observations and could prove to be detrimental for our analysis. Close to the seafloor we expect below critical Richardson numbers due to low stratification, and that was observed as well for most deployments. Observations of below critical values of the Richardson number can serve as a proxy for the vertical and subsequent horizontal transport of nutrients and other materials along the Florida shelf, so more research is needed to improve the current results in a much more meaningful capacity.

VII. Upwelling

Upwelling occurs when deep, cold, and nutrient rich water rises through the water column in response to diverging surface waters (Smith, 1983). Upwelling events can not only transport material from deep waters to the surface, but also alter productivity, displacement, and recruitment of biological activity (Hutchings et al., 1995; Kämpf & Chapman, 2016). Depending on their strength and persistence, upwelling events can be either beneficial or detrimental to coral reef ecosystems (Furnas, 2011). Coral reefs are able to develop and thrive in areas where upwelling is not intense or is intermittent, since the cold deep waters are usually at temperatures that are outside the corals' optimal range. Persistent and intense upwelling events can also enable the creation of diatom blooms, which in turn becomes detrimental for coral survivability. To analyze the possibility of upwelling events in this study, Pearson correlation coefficients were

calculated for the relationships between North velocity and the following variables: temperature, eastern velocity, depth, CDOM, and Chlorophyll. These were then divided into 5 distinct scenarios: all deployments, deployments when the SWF was absent, deployments when the SWF was present, deployments when the SWF appeared as an undercurrent, and deployments when the SWF appeared as a countercurrent.

All p-values for the Pearson correlation coefficients were below the significance level of 0.05, therefore all correlations are considered significant.

For all cases, north velocity and temperature have a significant positive moderate strength of association. Additionally, for all cases, north velocity and depth have a significant negative moderate strength of association. The strongest northern currents for almost all deployments were observed at the surface level, where temperatures are highest. As temperatures decrease with depth, and northern velocity was also observed to decrease with depth, these results are unsurprising and were actually expected. The surprising result is that the magnitude of the correlation coefficient between north velocity and depth is almost equal for the cases when the SWF is absent, when it is present, and when it is present as an undercurrent. It was expected that the undercurrent case would increase the strength of this correlation significantly, but that was not observed. A possible explanation is that for some deployments the SWF was present as both an undercurrent and a countercurrent. For those deployments, if the SWF was present as an undercurrent for a significant amount of time then it would still be included in the undercurrent case, regardless of whether it was also observed as a countercurrent at some point. Likewise, the opposite was also applied for the countercurrent case. It is a possibility that this inclusion might have helped diminish the strength of the correlation coefficient.

For all cases, north velocity and CDOM have a significant negative small to no strength of association. From the CTD results, it was observed that for most deployments CDOM concentrations peaked at the sea surface and close to the seafloor, with higher concentrations extending up to 60-80 m above the seafloor. Since high north velocities were observed at the surface, and only decreased with depth, it'd be expected that the correlation coefficient with CDOM would be low, since high CDOM concentrations were present at depths were north velocity was both at its maximum and at its minimum. The strongest correlation coefficient was found to be in the case when the SWF appeared as a countercurrent. This can be explained by

looking at the 3D plots and CTD contours. CDOM concentrations peaked across the entire water column when the glider moved close to the shore at shallower depths. It was also observed that when the SWF behaved as a countercurrent, it was mostly observed at shallower depths, in parts of the deployments when CDOM concentrations peaked, which would drive the correlation to be stronger. Since the weak negative association occurs when the southward flow appears as a countercurrent only, and the association is negligible when the only the undercurrent appears, or when the southward flow is missing, this could mean that CDOM is not necessarily restricted to deep water as previously thought, but is still being transported southwards to some slight degree.

For all cases, north velocity and chlorophyll have a significant positive small strength of association. This is as expected, since as observed from the optical channels contours chlorophyll concentrations peak just above the pycnocline. Consequently, this also might mean that the SWF is unable to transport primary producers with the exception of when it appears in its countercurrent form.

For all cases, north velocity and east velocity have a significant positive small to moderate strength of association. Eastward flow represents an offshore movement of water. A negative eastward flow, westward, represents onshore movement of water. The strongest correlation coefficient comes from the case when the SWF appeared as an undercurrent. In this case, it is known that northward flow is, mostly, restricted to upper part of the water column, while southward flow is restricted, mostly, to the deeper layers. Since it's a positive strength of association, then as northward flow increases, eastward flow does so as well. Consequently, as northward flow decreases until it becomes southwards, eastward flow decreases until it turns westward. This can be observed from Figure 23, where the average eastern component of the current velocity is plotted against the northern. With the undercurrent is present, westward (onshore) flow of water is likely to occur at depth, while eastward (offshore) flow of water is likely to occur close to the surface where Northern currents prevail. This type of flow would provide the optimal conditions for coastal upwelling events, since surface waters are being replaced by cold, nutrient rich, deep waters. The data presented here, however, is so far insufficient to corroborate whether they are actually taking place. More research is needed to establish whether these upwelling events are occurring and if they could alter nutrient dynamics and local biological interactions.

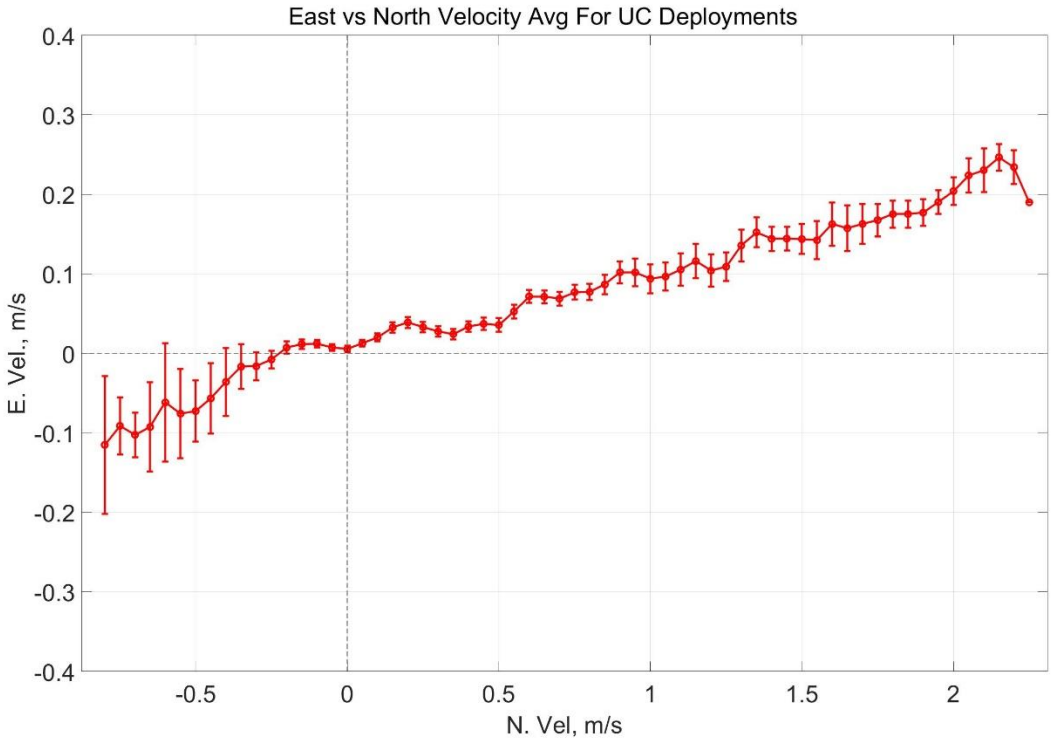

Figure 23. Averaged eastern and northern velocity components for the deployments when the SWF appeared as an undercurrent. The dashed black lines are the respective 0 m/s value for both components. Deployments used for analysis are scattered throughout 2022 and 2023.

8. Conclusions

The intercalibration of the glider and the Wirewalker provided good coherence both qualitatively and quantitatively. Additionally, Pearson correlation coefficients showed a strong strength of association between the north and eastern components of velocities, temperature, salinity, and density from both instruments. This goes on to show how both of these are good and useful oceanographic instruments for taking measurements of the physical aspects of the ocean in a high energy environment, such as the Gulf Stream.

Through the analysis of glider velocity patterns of different deployments spread throughout 2022 and 2023, we were able to find evidence of an intermittent SWF. This SWF in general portrayed characteristics of an undercurrent during the summer period and of a countercurrent during the winter period. Although still not fully understood, this characteristic is most likely due to seasonal differences in sea surface temperature and subsequent changes to the strength of water column stratification. Strength of the SWF was often found to be larger closer to the shore,

while the FC dominated offshore. Its appearance close to the shore was also typically associated with coastal ocean eddies generated by a strong shear between the SWF and the FC. According to our observations, the SWF and coastal eddies most likely behave as a coupled system.

The CTD and optical channels results showed the presence of a sea surface anomaly that is most likely associated with outflow from Port Everglades. This outflow appears to be a significant source of particulates and biological matter, which is driving increased rates of surface primary productivity. Nevertheless, at this point in time, it is unknown whether this increased productivity is detrimental or beneficial to the local ecosystem. More research is needed in this area. Optical channels results also showed that to a minor degree, the SWF might be transporting particulate and biological material at depth, but not the transport of primary producers. This most likely has impacts on nutrient transport and likely on trophic interactions.

Richardson number contours were, at best, inconclusive. Although the interface layer between the SWF and the FC does show increased turbulent activity caused by the shear between opposite flowing layers, but that is not a feature observed during all of the deployments. More research is needed to see how the SWF might be increasing turbulent flow and the vertical or horizontal transport of nutrients and particulates.

Finally, the optimal conditions that would allow the formation of upwelling events were observed to be taking place. These conditions are dependent on the SWF appearing as an undercurrent. The total capacity that the undercurrent has to drive these upwelling events, and how much upwelling actually is occurring, is at this time unknown. Future research should focus on discerning how much SWF is really necessary to trigger an upwelling event for accurate and safe planning of countermeasures and control.

More research is needed to accurately assess the effects the SWF and coastal eddies coupled system has on velocities, transport, mixing, and upwelling along and across the shelf.

9. Limitations and Future Steps

The current project suffers from several limitations. First, the gilder deployments suffer from being too short, which prevents any significant large-scale variability from being observed in the resulting data. Information on spatial and temporal large-scale phenomena, such as mesoscale

eddies, tidal variability, climatic conditions, etc., could provide some additional insight into the observed patterns of the SWF. Additionally, longer deployments require a significant amount of active piloting time, which is not feasible with our current setup. Second, the intercalibration of the glider and the Wirewalker only had available data for a relatively small window when compared to the overall length of the deployments. Unfortunately, the Wirewalker buoy system was lost at sea after an unexpected collision with a ship and subsequent sinking of the buoy. Nevertheless, a new buoy is in the process of being purchased so that future Wirewalker deployments are possible. Third, the LADCP procedure outputs LADCP profiles that it tries to match to the bottom tracking profiles as best as it can, but when not possible, a manual correction has to be applied. This leaves the final plots vulnerable to human bias, as they are matched by visual acuity only. Finally, the conditions of the western flank of the Gulf Stream and the local climate severely restricted the amount of glider deployments we were able to do. A possible approach to deal with this would be to establish long-term monitoring stations to get a more complete dataset even through harsh conditions.

References

Anderson, D. L., & Corry, R. A. (1985). Seasonal transport variations in the Florida Straits: A model study. *Journal of Physical Oceanography*, *15*(6), 773-786. 10.1175/1520-0485(1985)015<0773:stvitf>2.0.co;2.

Baringer, M. O. N., & Larsen, J. C. (2001). Sixteen years of Florida Current transport at 27 N. *Geophysical Research Letters*, *28*(16), 3179-3182. 10.1029/2001GL013246.

Britannica (2015, October 28). Water mass. *Encyclopedia Britannica*. https://www.britannica.com/science/water-mass

Brown, N. (1974, August). A precision CTD microprofiler. In *Ocean'74-IEEE International Conference on Engineering in the Ocean Environment* (pp. 270-278). IEEE. 10.1109/OCEANS.1974.1161443.

Brown, N. L., & Morrison, G. K. (1978). *WHOI/Brown conductivity, temperature, and depth microprofiler* (p. 0271). Woods Hole Oceanographic Institution.

Brumley, B. H., Cabrera, R. G., Deines, K. L., & Terray, E. A. (1991). Performance of a broad-band acoustic Doppler current profiler. *IEEE Journal of Oceanic Engineering*, *16*(4), 402-407. 10.1109/48.90905.

Candela, J., Sheinbaum, J., Ochoa, J., Badan, A., & Leben, R. (2002). The potential vorticity flux through the Yucatan Channel and the Loop Current in the Gulf of Mexico. *Geophysical Research Letters*, *29*(22), 16-1. 10.1029/2002GL015587.

Carr, S. D., Capet, X. J., McWilliams, J. C., Pennington, J. T., & Chavez, F. P. (2008). The influence of diel vertical migration on zooplankton transport and recruitment in an upwelling region: Estimates from a coupled behavioral-physical model. *Fisheries Oceanography*, *17*(1), 1-15. 10.1111/j.1365-2419.2007.00447.x.

Chelton, D. B., Schlax, M. G., Samelson, R. M., & de Szoeke, R. A. (2007). Global observations of large oceanic eddies. *Geophysical Research Letters*, *34*(15). 10.1029/2007GL030812.

Del Mar Oceanographic, LLC (n.d.). *Wirewalker how it works*. Del Mar Ocean. https://www.delmarocean.com/ww-how-it-works

Dortch, Q. (2018). *West Florida Shelf and dry tortugas impact Gulf of Mexico loop current.* NCCOS Coastal Science. https://coastalscience.noaa.gov/news/west-florida-shelf-and-dry-tortugas-impact-gulf-of-mexico-loop-current/

Düing, W., & Johnson, D. (1971). Southward flow under the Florida Current. *Science*, *173*(3995), 428-430. 10.1126/science.173.3995.428.

Fiechter, J., & Mooers, C. N. K. (2007). Primary production associated with the Florida Current along the East Florida Shelf: Weekly to seasonal variability from mesoscale-resolution biophysical simulations. *Journal of Geophysical Research: Oceans*, *112*(C12). 10.1029/2006JC003576.

Furnas, M. J. (2011). Upwelling and coral reefs. In D. Hopley (Ed.), *Encyclopedia of Modern Coral Reefs: Structure, Form, and Process* (pp. 1125-1132). Springer. 10.1007/978-90-481-2639-2_160

Gafurov, S. A., & Klochkov, E. V. (2015). Autonomous unmanned underwater vehicles development tendencies. *Procedia Engineering*, *106*, 141-148. 10.1016/j.proeng.2015.06.017.

Galperin, B., Sukoriansky, S., & Anderson, P. S. (2007). On the critical Richardson number in stably stratified turbulence. *Atmospheric Science Letters*, *8*(3), 65-69. 10.1002/asl.153.

Gardner, W. D., Richardson, M. J., & Cacchione, D. A. (1989). Sedimentological effects of strong southward flow in the Straits of Florida. *Marine Geology*, *86*(2-3), 155-180. 10.1016/0025-3227(89)90047-9

Gotvald, A. J., & Oberg, K. A. (2009). *Acoustic Doppler current profiler applications used in rivers and estuaries by the US Geological Survey* (No. 2008-3096). US Geological Survey. 10.3133/FS20083096.

Gradone, J. C., Hunter, E. J., Mullison, J., & Miles, T. N. (2021, September). Development of onboard processing capabilities for a Slocum glider acoustic doppler current profiler. In *OCEANS 2021: San Diego–Porto* (pp. 1-5). IEEE. 10.23919/OCEANS44145.2021.9705895.

Huvenne, V. A., Robert, K., Marsh, L., Lo Iacono, C., Le Bas, T., & Wynn, R. B. (2018). ROVs and AUVs. In A. Micallef, S. Krastel, & A. Savini (Eds.), *Submarine geomorphology* (pp. 93-108). Springer. 10.1007/978-3-319-57852-1_7

Hutchings, L., Pitcher, G. C., Probyn, T. A., & Bailey, G. W. (1995). The chemical and biological consequences of coastal upwelling. *Environmental Sciences Research Report Es*, *18*, 65-82.

IKM 3D Animation Services. (2020). *Teledyne Marine – Slocum G3 Glider Animation* [Video]. Youtube. https://www.youtube.com/watch?v=1RwL9b5IJsA

Javaid, M. Y., Ovinis, M., Nagarajan, T., & Hashim, F. B. (2014). Underwater gliders: A review. *MATEC Web of Conferences, 13, 02020*. 10.1051/matecconf/20141302020.

Kämpf, J., & Chapman, P. (2016). *Upwelling systems of the world*. Springer International Publishing Switzerland. 10.1007/978-3-319-42524-5.

Kourafalou, V. H., & Kang, H. (2012). Florida Current meandering and evolution of cyclonic eddies along the Florida Keys Reef Tract: Are they interconnected? *Journal of Geophysical Research: Oceans*, *117*(C5). 10.1029/2011JC007383.

Leaman, K. D., & Molinari, R. L. (1987). Topographic modification of the Florida Current by Little Bahama and Great Bahama Banks. *Journal of Physical Oceanography*, *17*(10), 1724-1736. 10.1175/1520-0485(1987)017<1724:TMOTFC>2.0.CO;2.

Lee, T. N. (1975, November). Florida Current spin-off eddies. *Deep Sea Research and Oceanographic Abstracts, 22*(11), 753-765. 10.1016/0011-7471(75)90080-7.

Ludvigsen, M., Johnsen, G., Sørensen, A. J., Lågstad, P. A., & Ødegård, Ø. (2014). Scientific operations combining ROV and AUV in the Trondheim Fjord. *Marine Technology Society Journal*, *48*(2), 59-71. 10.4031/MTSJ.48.2.3.

Niiler, P. P., & Richardson, W. S. (1973). Seasonal variability of the Florida Current. *Journal of Marine Research, 31*(3), 144-167.

Oey, L., Ezer, T., & Lee, H. (2005). Loop Current, rings and related circulation in the Gulf of Mexico: A review of numerical models and future challenges. *Geophysical Monograph-American Geophysical Union, 161*, 31. 10.1029/161GM04.

Ordonez, C. E., Shearman, R. K., Barth, J. A., Welch, P., Erofeev, A., & Kurokawa, Z. (2012, May). Obtaining absolute water velocity profiles from glider-mounted Acoustic Doppler Current Profilers. In *2012 Oceans-Yeosu* (pp. 1-7). IEEE. 10.1109/OCEANS-Yeosu.2012.6263582.

Otis, D. B., Le Hénaff, M., Kourafalou, V. H., McEachron, L., & Muller-Karger, F. E. (2019). Mississippi River and Campeche Bank (Gulf of Mexico) episodes of cross-shelf export of coastal waters observed with satellites. *Remote Sensing*, *11*(6), 723. 10.3390/rs11060723.

Pérez-Brunius, P., Furey, H., Bower, A., Hamilton, P., Candela, J., García-Carrillo, P., & Leben, R. (2018). Dominant circulation patterns of the deep Gulf of Mexico. *Journal of Physical Oceanography*, *48*(3), 511-529. 10.1175/JPO-D-17-0140.1.

Pettigrew, N., & Irish, J. (1983, August). An evaluation of a bottom-mounted Doppler acoustic profiling current meter. In *Proceedings OCEANS'83* (pp. 182-186). IEEE.

Robinson, A. R. (Ed.). (1983). *Eddies in marine science*. Springer Science & Business Media. 10.1007/978-3-642-69003-7.

Rudnick, D. L. (2016). Ocean research enabled by underwater gliders. *Annual Review of Marine Science*, *8*, 519-541. 10.1146/annurev-marine-122414-033913.

Sahoo, A., Dwivedy, S. K., & Robi, P. S. (2019). Advancements in the field of autonomous underwater vehicle. *Ocean Engineering*, *181*, 145-160. 10.1016/j.oceaneng.2019.04.011.

Schmitz Jr, W. J., & Richardson, W. S. (1968, December). On the transport of the Florida Current. *Deep Sea Research and Oceanographic Abstracts, 15*(6), 679-693. 10.1016/0011-7471(68)90081-8.

Schott, F. A., Lee, T. N., & Zantopp, R. (1988). Variability of structure and transport of the Florida Current in the period range of days to seasonal. *Journal of Physical Oceanography*, *18*(9), 1209-1230. 10.1175/1520-0485(1988)018<1209:VOSATO>2.0.CO;2.

Shulzitski, K., Sponaugle, S., Hauff, M., Walter, K. D., & Cowen, R. K. (2016). Encounter with mesoscale eddies enhances survival to settlement in larval coral reef fishes. *Proceedings of the National Academy of Sciences*, *113*(25), 6928-6933. 10.1073/pnas.1601606113.

Siegel, E. (2009). Capabilities for gliders. *Marine Technology Reporter*, 28-34.

Smith, N. P. (1981). An investigation of seasonal upwelling along the Atlantic coast of Florida. In *Elsevier Oceanography Series* (Vol. 32, pp. 79-98). Elsevier. 10.1016/S0422-9894(08)70405-7.

Smith, Robert L. (1983). *Physical features of coastal upwelling systems*. Washington Sea Grant.

Soloviev, A. V., Hirons, A., Maingot, C., Dean, C. W., Dodge, R. E., Yankovsky, A. E., Wood, J., Weisberg, R.H., Luther, M.E. & McCreary, J. P. (2017). Southward flow on the western flank of the Florida Current. *Deep Sea Research Part I: Oceanographic Research Papers*, *125*, 94-105. 10.1016/j.dsr.2017.05.002.

Sponaugle, S., Lee, T., Kourafalou, V., & Pinkard, D. (2005). Florida Current frontal eddies and the settlement of coral reef fishes. *Limnology and Oceanography*, *50*(4), 1033-1048. 10.4319/lo.2005.50.4.1033.

Stommel, H. (1965). *The Gulf Stream: A physical and dynamical description*. Univ of California Press.

Todd, R. E., Rudnick, D. L., Sherman, J. T., Owens, W. B., & George, L. (2017). Absolute velocity estimates from autonomous underwater gliders equipped with Doppler current profilers. *Journal of Atmospheric and Oceanic Technology*, *34*(2), 309-333. 10.1175/JTECH-D-16-0156.1.

Wynn, R. B., Huvenne, V. A., Le Bas, T. P., Murton, B. J., Connelly, D. P., Bett, B. J., Ruhl, H. A., Morris, K. J., Peakall, J., Parsons, D. R., Sumner, E. J., Darby S. E., Dorrell, R. M., & Hunt, J. E. (2014). Autonomous underwater vehicles (AUVs): Their past, present and future contributions to the advancement of marine geoscience. *Marine Geology*, *352*, 451-468. 10.1016/j.margeo.2014.03.012.

Yeung, C., Jones, D. L., Criales, M. M., Jackson, T. L., & Richards, W. J. (2001). Influence of coastal eddies and counter-currents on the influx of spiny lobster, Panulirus argus, postlarvae into Florida Bay. *Marine and Freshwater Research*, *52*(8), 1217-1232. 10.1071/MF01110.

Zantopp, R. J., Leaman, K. D., & Lee, T. N. (1987). Florida Current meanders: a close look in June–July 1984. *Journal of Physical Oceanography*, *17*(5), 584-595. 10.1175/1520-0485(1987)017<0584:FCMACL>2.0.CO;2.

Zhang, R., Yang, S., Wang, Y., Wang, S., Gao, Z., & Luo, C. (2020). Three-dimensional regional oceanic element field reconstruction with multiple underwater gliders in the Northern South China Sea. *Applied Ocean Research*, *105*, 102405. 10.1016/j.apor.2020.102405.

Zhang, Y., Hu, C., Liu, Y., Weisberg, R. H., & Kourafalou, V. H. (2019). Submesoscale and mesoscale eddies in the Florida Straits: Observations from satellite ocean color measurements. *Geophysical Research Letters*, *46*(22), 13262-13270. 10.1029/2019GL083999.

Zhang, Z., & Qiu, B. (2020). Surface chlorophyll enhancement in mesoscale eddies by submesoscale spiral bands. *Geophysical Research Letters*, *47*(14), e2020GL088820. 10.1029/2020GL088820.

Zheng, B., Lucas, A. J., Pinkel, R., & Le Boyer, A. (2022). Fine-Scale Velocity Measurement on the Wirewalker Wave-Powered Profiler. *Journal of Atmospheric and Oceanic Technology*, *39*(2), 133-147. 10.1175/JTECH-D-21-0048.1.

10. Appendix A: Glider ADCP Figures

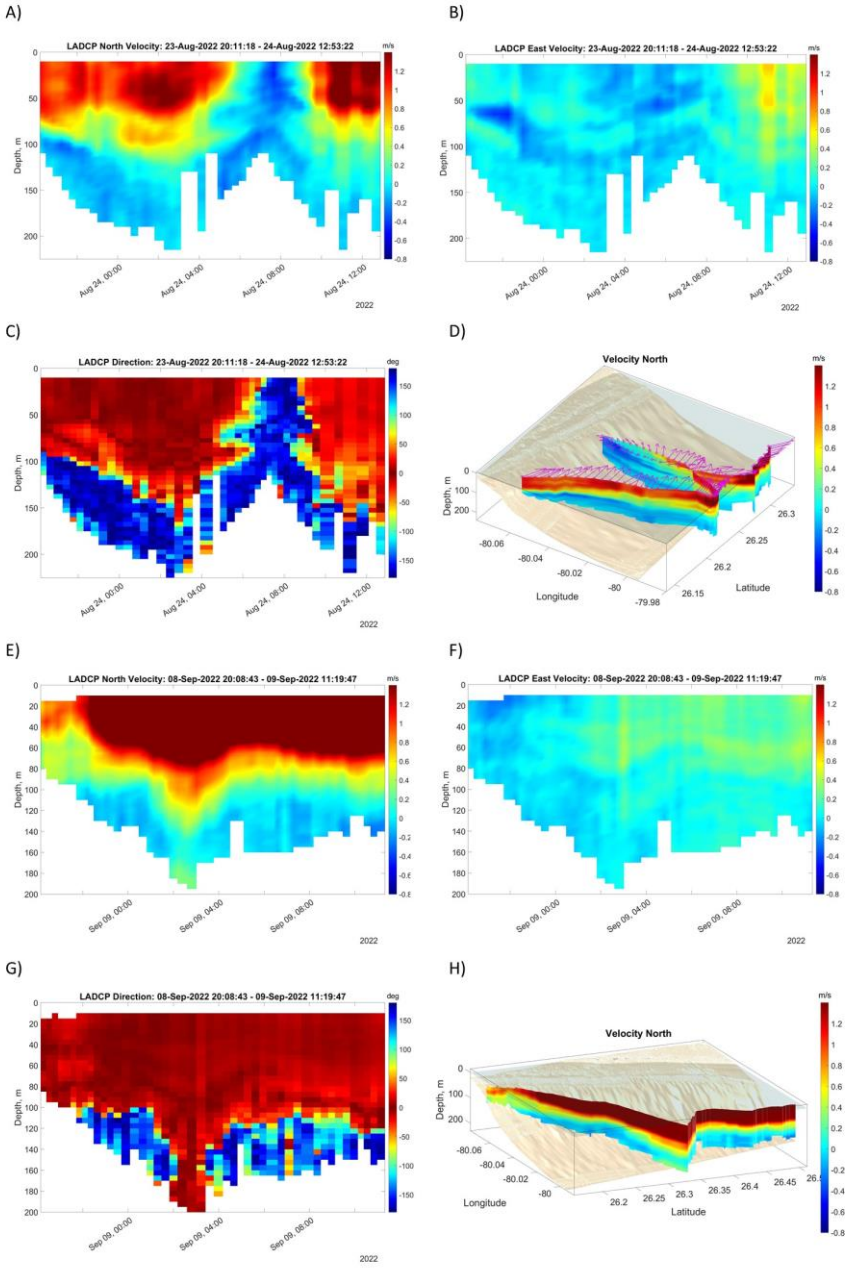

Figure A.1. LADCP figures for the August 23-24, 2022 deployment (A.1A, B, C, and D) and for the September 8-9, 2022 deployment (A.1E, F, G, and H). Y-axis in all plots represents depth, x-axis represents time, and the color bar represents current velocity in m/s or degree of direction, with 0 degrees being full northward flow. 3D plot shows the 20 m depth bin vector plot.

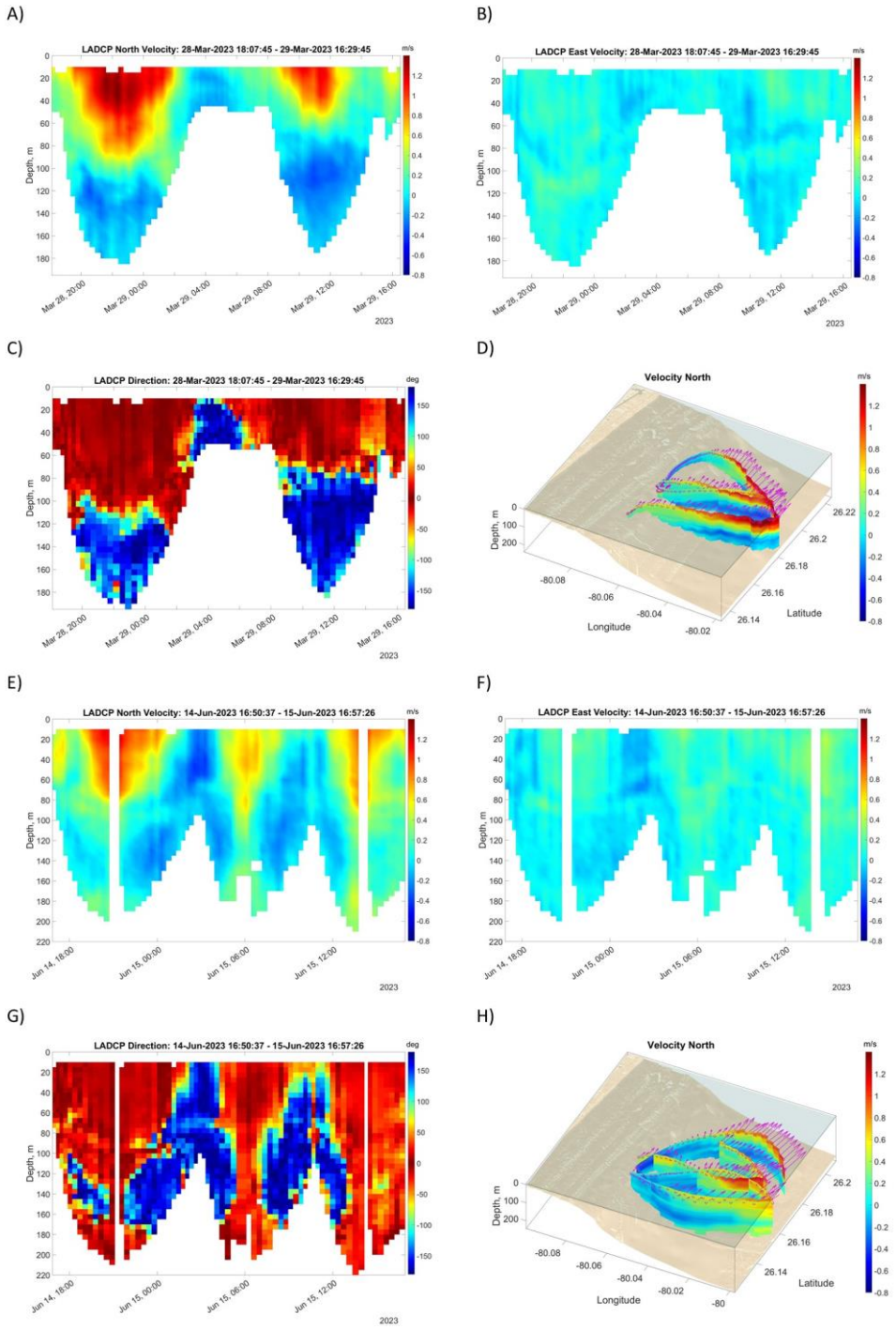

Figure A.2. LADCP figures for the March 28-29, 2023 deployment (A.2A, B, C, and D) and for the June 14-15, 2023 deployment (A.2E, F, G, and H). Y-axis in all plots represents depth, x-axis represents time, and the color bar represents current velocity in m/s or degree of direction, with 0 degrees being full northward flow. 3D plot shows the 20 m depth bin vector plot.

11. Appendix B: Glider CTD Figures

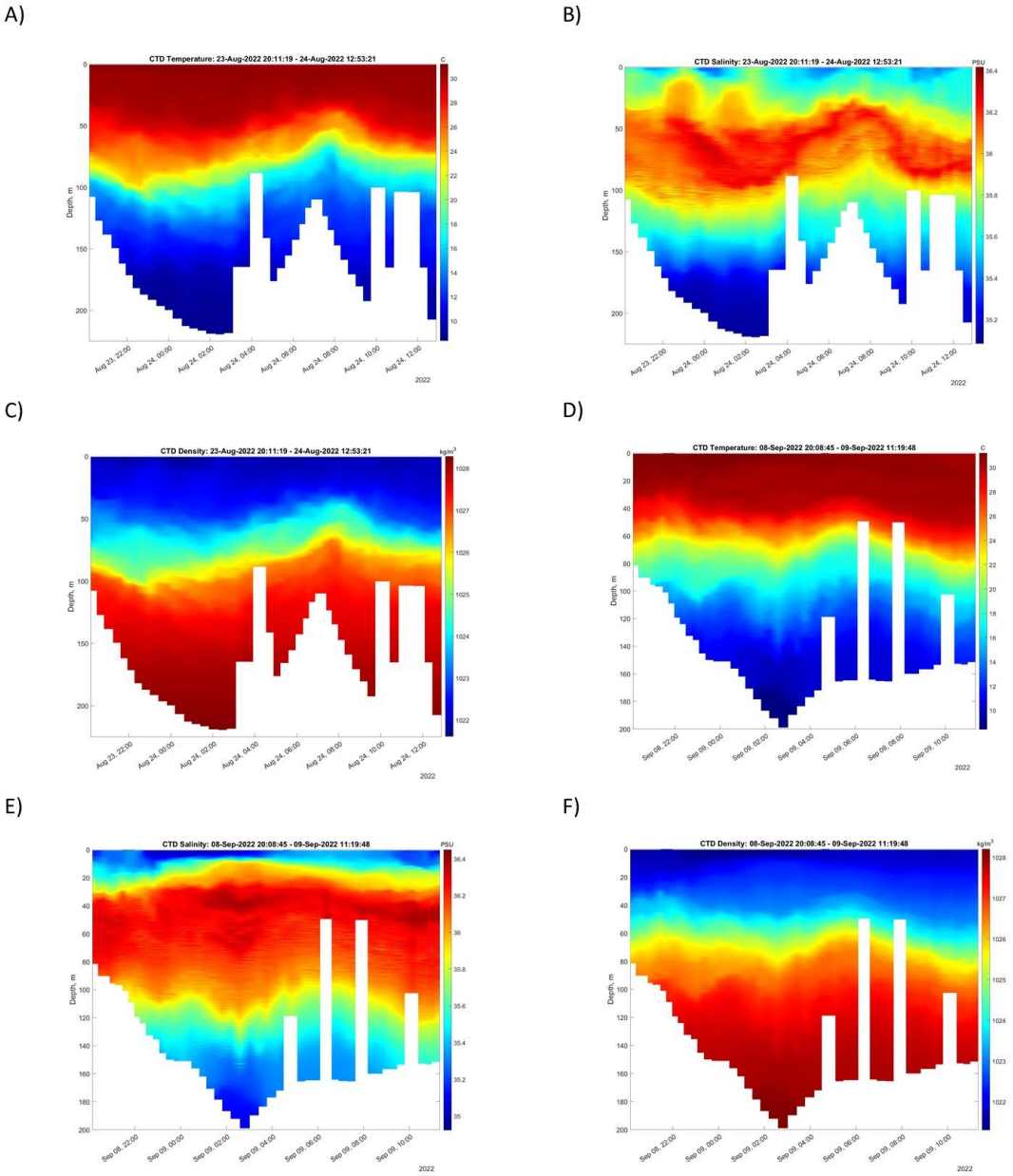

Figure B.1. CTD figures for the August 23-24, 2022 deployment (B.1A, B and C) and for the September 8-9, 2022 deployment (B.1D, E, and F). Y-axis in all plots represents depth, x-axis represents time, and the color bar represents the measurements (temperature, salinity, or density). Units are °C for temperature, PSU for salinity, and kg/m^3 for density.

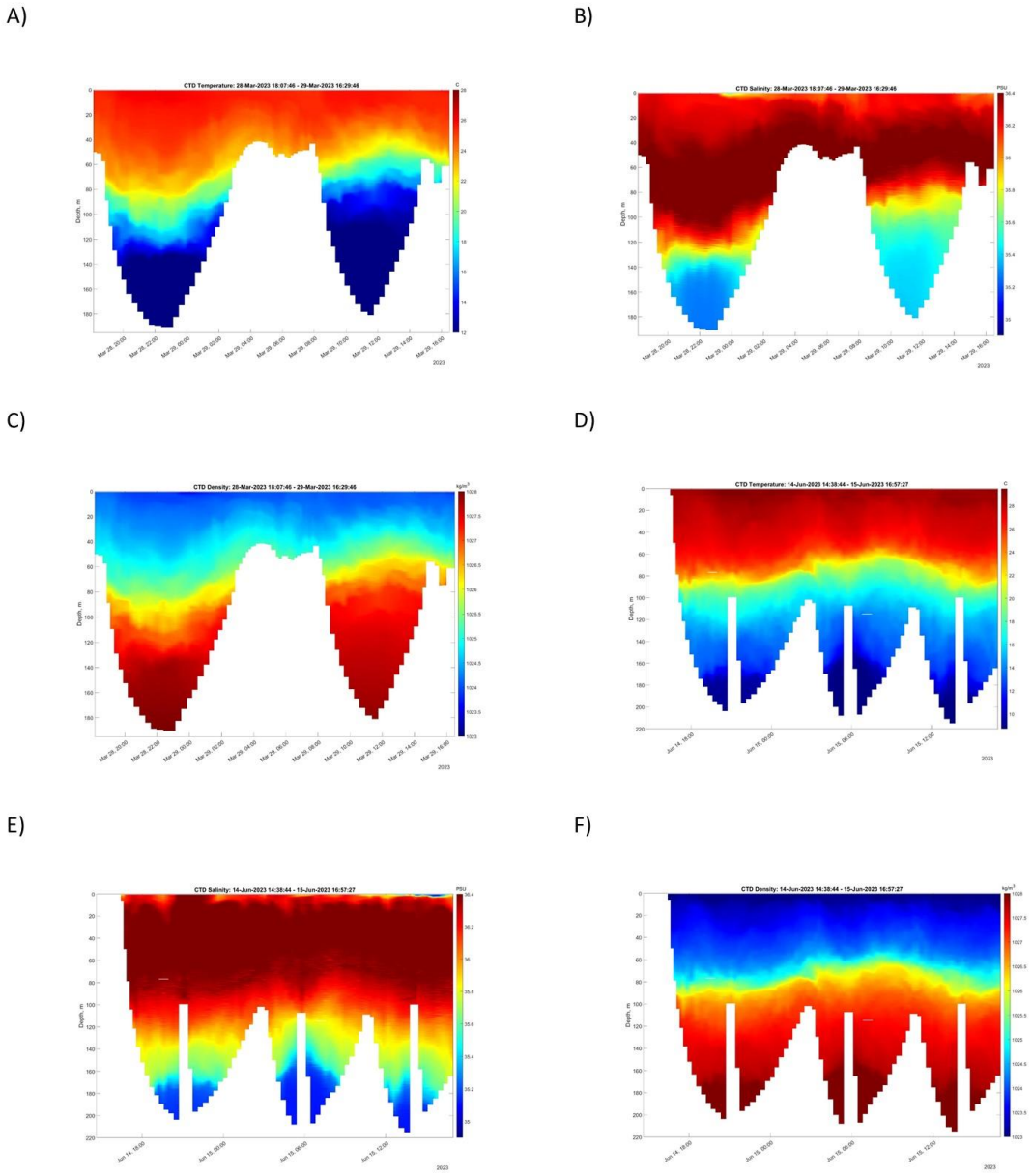

Figure B.2. CTD figures for the March 28-29, 2023 deployment (B.2A, B and C) and for the June 14-15, 2023 deployment (B.2D, E, and F). Y-axis in all plots represents depth, x-axis represents time, and the color bar represents the measurements (temperature, salinity, or density). Units are °C for temperature, PSU for salinity, and kg/m^3 for density.

12. Appendix C: Glider Optics Figures

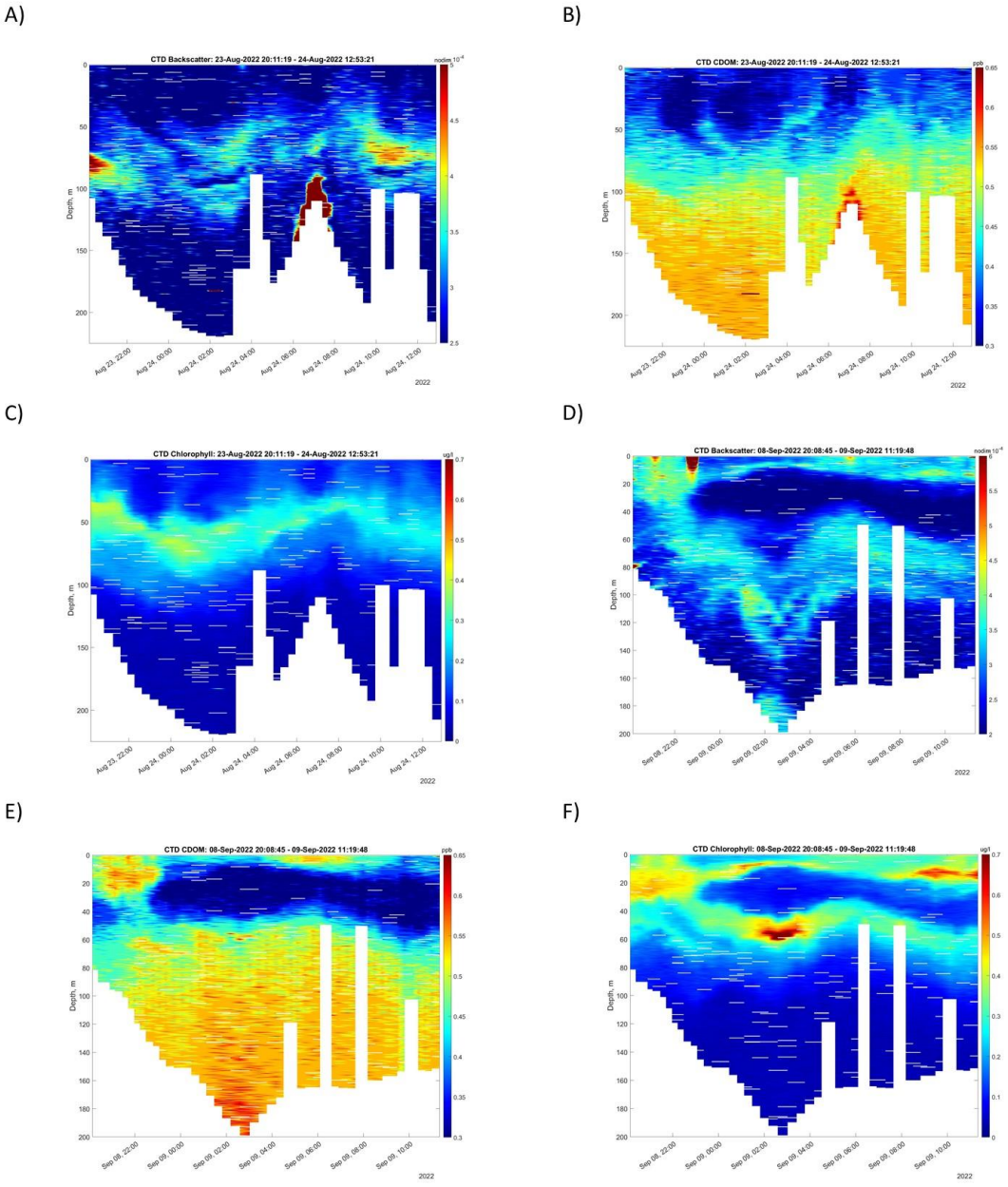

Figure C.1. Optic channels figures for the August 23-24, 2022 deployment (C.1A, B and C) and for the September 8-9, 2022 deployment (C.1D, E, and F). Y-axis in all plots represents depth, x-axis represents time, and the color bar represents the measurements (backscatter, CDOM, or chlorophyll concentrations). Units are counts for backscatter, ppb for CDOM, and µg/L for chlorophyll.

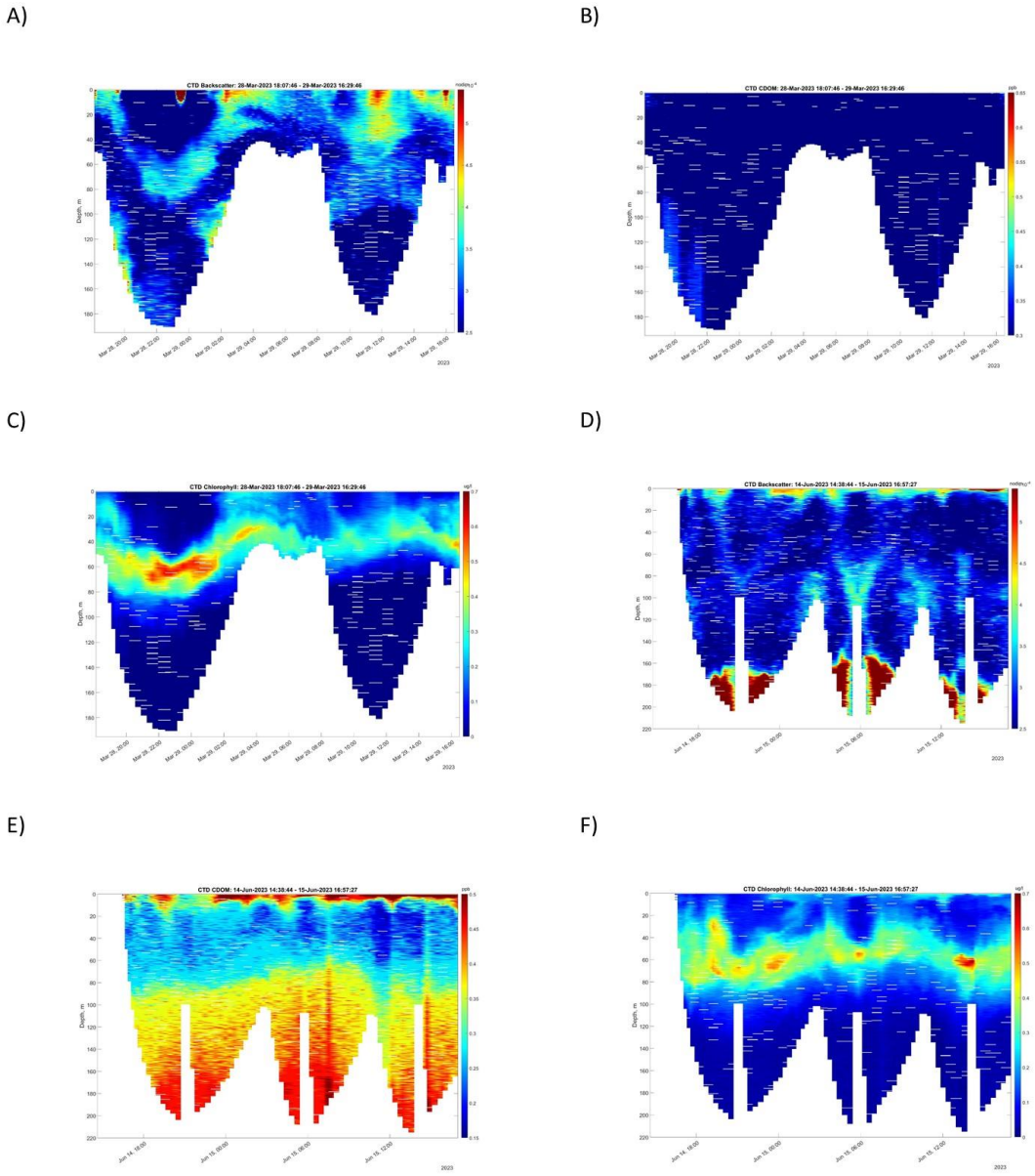

Figure C.2. CTD figures for the March 28-29, 2023 deployment (C.2A, B and C) and for the June 14-15, 2023 deployment (C.2D, E, and F). Y-axis in all plots represents depth, x-axis represents time, and the color bar represents the measurements (backscatter, CDOM, or chlorophyll concentrations). Units are counts for backscatter, ppb for CDOM, and µg/L for chlorophyll.

13. Appendix D: Glider Richardson Figures

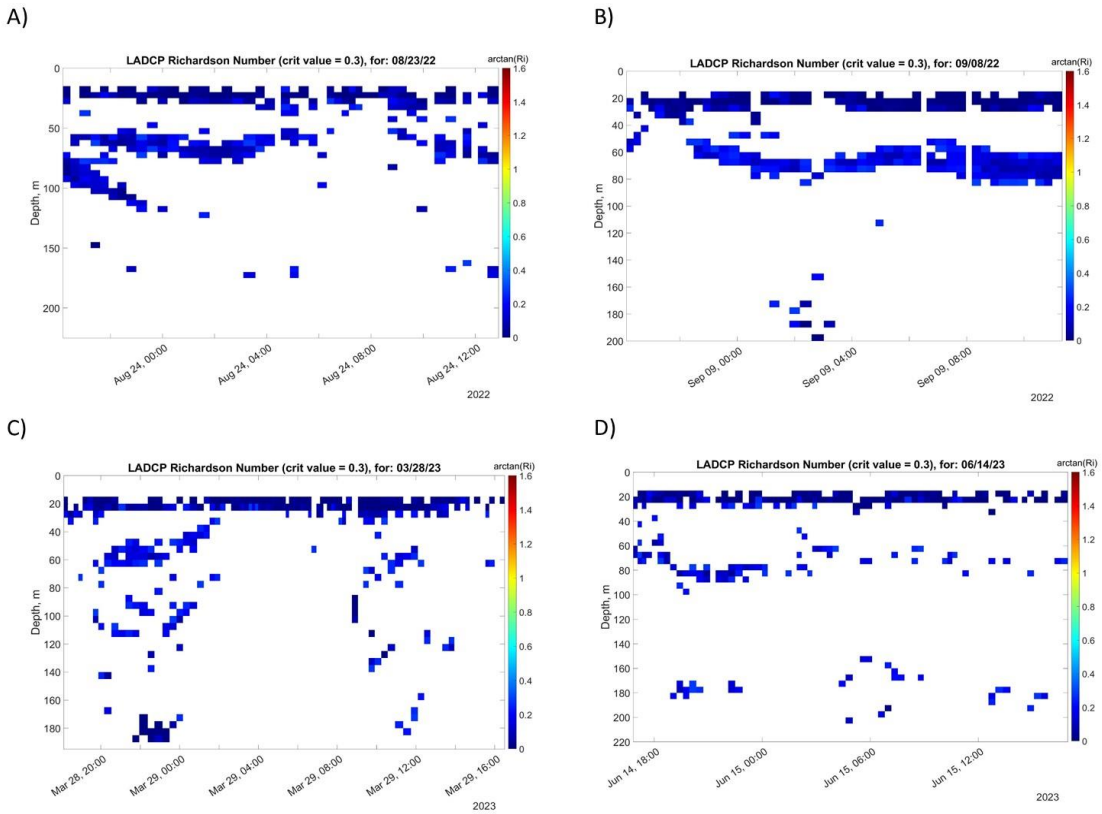

Figure D.1. Richardson number contours for the August 23-24, 2022 deployment, D.1A, the September 8-9, 2022 deployment, D.1B, the March 28-29, 2023 deployment, D.1C, and for the June 14-15, 2023 deployment, D.1D. Y-axis in all plots represents depth, x-axis represents time, and the color bar represents the arctan of the Richardson number, Ri. Actual contour only shows cells where the Richardson number was found to be below the critical value of 0.3.

14.Appendix E: Tables

Table E.1. The table shows minimum, maximum, and average values for the surface (top 20 m) and bottom (last 20 m) layers for each deployment for temperature, salinity, and density. The deployment names represent the dates when the glider was in the ocean, and are written in the format of YYYYMMDD_YYYYMMDD. Rows are color coded depending on which season each deployment took part in. Yellow represents spring, orange represents summer, green represents fall, and blue represents winter. Units are °C for temperature, PSU for salinity, and kg/m^3 for density. Averages are calculated using all available data for each deployment.

Deployment	Min. Surf. Temp.	Max. Surf. Temp.	Avg. Surf. Temp.	Min. Surf. Sal.
20220401_20220403	24.17	25.85	24.91	36.05
20220610_20220613	26.64	28.27	27.63	34.57
20220719_20220720	30.00	30.57	30.25	36.11
20220801_20220803	19.81	30.17	29.02	35.95
20220818_20220819	29.91	30.90	30.30	35.37
20220823_20220824	30.26	31.18	30.57	35.38
20220908_20220909	30.22	31.20	30.68	34.92
20220914_20220915	29.94	31.12	30.68	34.17
20221010_20221011	28.20	28.91	28.47	35.26
20221026_20221027	27.28	27.89	27.66	35.50
20221101_20221102	27.57	28.25	27.83	35.86
20221116_20221117	27.42	27.96	27.76	35.79
20221206_20221207	26.81	27.22	27.06	35.92
20221208_20221209	26.66	26.95	26.85	35.94
20221213_20221214	26.56	26.97	26.74	35.76
20230131_20230201	25.81	26.71	26.03	1.55
20230223_20230224	23.81	26.59	25.07	35.52
20230307	24.44	25.93	25.27	36.11
20230328_20230329	24.59	26.12	25.46	35.65
20230614_20230615	27.63	29.49	28.58	35.06
20230620_20230623	27.57	34.36	28.67	0.01
20230808_20230810	21.76	31.74	29.06	35.23
20230919_20230921	29.40	31.27	30.53	34.03

Max. Surf. Sal.	Avg. Surf. Sal.	Min. Surf. Dens.	Max. Surf. Dens.	Avg. Surf. Dens.	Min. Bot. Temp.	Max. Bot. Temp.
36.34	36.28	1024.03	1024.68	1024.38	11.24	22.43
36.24	35.91	1022.17	1023.84	1023.25	14.36	25.77
36.26	36.16	1022.41	1022.75	1022.56	13.60	26.91
36.47	36.23	1022.59	1025.66	1023.02	9.48	29.72
35.78	35.61	1021.82	1022.40	1022.13	8.57	30.21
36.03	35.65	1021.61	1022.43	1022.06	8.39	24.07
36.08	35.52	1021.31	1022.51	1021.93	8.43	30.49
36.26	35.26	1020.88	1022.53	1021.74	9.58	30.57
35.83	35.64	1022.38	1022.96	1022.77	9.39	26.67
35.92	35.85	1022.87	1023.29	1023.19	13.74	27.75
36.14	35.99	1023.02	1023.46	1023.24	12.26	27.68
36.09	36.04	1023.02	1023.47	1023.30	11.78	27.84
36.02	36.00	1023.41	1023.60	1023.50	10.16	26.95
36.05	36.00	1023.46	1023.66	1023.57	9.88	26.85
36.11	36.04	1023.40	1023.71	1023.63	10.80	26.72
35.93	35.89	997.88	1023.85	1023.75	11.97	26.19
36.22	35.95	1023.56	1024.69	1024.08	7.79	20.68
36.44	36.34	1023.99	1024.68	1024.32	10.08	23.88
36.38	36.22	1023.58	1024.59	1024.17	10.03	25.32
36.50	36.31	1022.10	1023.68	1023.24	8.72	26.59
36.48	36.10	994.27	1023.67	1023.05	9.60	27.45
36.57	36.14	1021.71	1025.42	1022.93	9.50	26.01
36.12	35.20	1020.87	1022.59	1021.74	9.96	30.42

Avg. Bot. Temp.	Min. Bot. Sal.	Max. Bot. Sal.	Avg. Bot. Sal.	Min. Bot. Dens.	Max. Bot. Dens.	Avg. Bot. Dens.
18.03	35.46	36.36	36.11	1025.42	1027.68	1026.48
18.39	35.89	36.40	36.22	1024.29	1027.34	1026.51
19.26	35.79	36.41	36.11	1024.08	1027.37	1026.15
24.19	35.23	36.34	36.05	1022.74	1027.79	1024.34
14.76	35.09	36.25	35.64	1022.33	1028.22	1026.93
11.26	35.08	36.32	35.43	1024.88	1028.29	1027.74
12.93	35.10	36.37	35.58	1022.52	1028.20	1027.37
18.96	35.00	36.49	35.85	1021.56	1028.04	1025.92
16.00	35.21	36.66	36.03	1024.20	1028.33	1027.25
19.45	35.69	36.66	36.16	1023.02	1027.89	1026.29
20.48	35.61	36.65	36.17	1023.25	1028.02	1026.00
21.36	35.53	36.70	36.12	1023.26	1028.09	1025.57
19.48	35.32	36.62	36.14	1023.48	1028.18	1026.22
18.40	35.24	36.69	36.11	1023.54	1028.24	1026.53
19.74	35.36	36.66	36.04	1023.60	1028.20	1026.05
24.54	35.58	36.26	35.92	1023.69	1027.80	1024.30
11.35	34.73	36.35	35.31	1025.88	1028.44	1027.55
16.41	35.36	36.49	36.12	1024.91	1027.98	1027.07
17.50	35.26	36.49	35.98	1024.31	1028.01	1026.42
12.54	35.11	36.48	35.62	1024.20	1028.24	1027.61
17.51	35.19	36.45	36.10	1023.77	1028.18	1026.59
14.29	35.21	36.43	35.87	1024.18	1028.18	1027.30
18.68	35.26	36.54	36.13	1021.97	1028.06	1026.34

Table E.2. The table shows average values for the surface (top 20 m) and bottom (last 20 m) layers for temperature, salinity, and density for each season for when glider data is available. Units are °C for temperature, PSU for salinity, and kg/m^3 for density.

Averages	Surf. Temp.	Surf. Sal.	Surf. Dens.	Bot. Temp.	Bot. Sal.	Bot. Dens.
Spring 2022	26.54	36.06	1023.70	18.24	36.18	1026.50
Summer 2022	29.95	35.84	1022.42	18.60	35.83	1025.92
Fall 2022	27.92	35.89	1023.14	19.45	36.12	1026.24
Winter 2022/23	26.25	35.99	1023.75	18.55	35.91	1026.18
Spring 2023	25.46	36.22	1024.17	17.50	35.98	1026.42
Summer 2023	28.76	36.16	1023.06	15.50	35.93	1027.02
Fall 2023	30.53	35.20	1021.74	18.68	36.13	1026.34

Table E.3. The table shows minimum, maximum, and average values for the surface (top 20 m) and bottom (last 20 m) layers for each deployment for backscatter, CDOM, and chlorophyll concentrations. The deployment names represent the dates when the glider was in the ocean, and are written in the format of YYYYMMDD_YYYYMMDD. Rows are color coded depending on which season each deployment took part in. Yellow represents spring, orange represents summer, green represents fall, and blue represents winter. Units are none for backscatter, parts per billion (ppb) for CDOM, and µg/L for chlorophyll. Averages are calculated using all available data for each deployment.

Deployment	Min. Surf. Back.	Max. Surf. Back.
20220401_20220403	0.00022134	0.00300576
20220610_20220613	0.0003318	0.00085467
20220719_20220720	0.00031806	0.00105369
20220801_20220803	0.000273849	0.00659295
20220818_20220819	0.0001767	0.001065188
20220823_20220824	0.00017577	0.0005115
20220908_20220909	0.00018414	0.00424368
20220914_20220915	0.00018228	0.00066942
20221010_20221011	0.00019344	0.00045151
20221026_20221027	0.00017484	0.00056466
20221101_20221102	0.00014601	0.00069564
20221116_20221117	0.00016554	0.0006231
20221206_20221207	0.00015996	0.00040734
20221208_20221209	0.00019251	0.00052638
20221213_20221214	0.00018228	0.00322896
20230131_20230201	0.0002139	0.00531681
20230223_20230224	0.00022568	0.00285972
20230307	0.00018972	0.00068570
20230328_20230329	0.000182	0.004534
20230614_20230615	0.000203	0.000761
20230620_20230623	0.000227	0.007602
20230808_20230810	0.000192	0.00061
20230919_20230921	0.000219	0.004407

Avg. Surf. Back.	Min. Surf. CDOM	Max. Surf. CDOM	Avg. Surf. CDOM	Min. Surf. Chlor.	Max. Surf. Chlor.	Avg. Surf. Chlor.
0.000428967	0.226	0.981485714	0.452905241	0.0365	0.5037	0.289877176
0.000426471	-2.605163636	2.692225	0.572098851	0.09125	1.374833333	0.330064043
0.000399738	-0.1808	0.904	0.393821513	0.05475	0.4234	0.123183598
0.000346822	0.194707692	2.229866667	0.416424986	0.0657	0.742166667	0.258405897
0.000257932	0.226	0.645714286	0.375090245	0.0438	0.3212	0.163003626
0.000239381	-0.10848	0.787233333	0.341607297	0.0438	0.2409	0.12259429
0.000339508	0.2712	0.7232	0.406914647	0.0876	0.7373	0.327642528
0.000364299	0.241066667	0.7232	0.448385548	0.165466667	0.8541	0.449964763
0.000226576	0.1808	0.75032	0.320998312	0.035283333	0.6643	0.148368778
0.000237266	0.0904	0.65088	0.30389747	0.04015	0.5986	0.157588452
0.000273231	0.030133333	0.452	0.259421198	-0.04015	0.4307	0.145135233
0.000215752	0.1808	0.452	0.263443706	0.0219	0.326675	0.089188586
0.000194267	-0.120533333	0.730153846	0.279783371	0.0584	0.238466667	0.118388732
0.000233974	0.187594771	0.544051142	0.294465589	0.0511	0.3431	0.132113056
0.000236647	0.115413592	0.559837563	0.291273555	0.01825	0.476933333	0.108130302
0.000406856	0.1808	167.346087	0.377076642	0.073	1.233065217	0.206854902
0.000358454	0.0452	1.074369231	0.360246186	0.04015	0.450073077	0.147702838
0.000220683	0.0904	0.518610526	0.18379984	-0.0073	0.1606	0.037599857
0.00034	0.007533	0.499165	0.123374	-0.0511	0.46355	0.136975
0.000314	0.0904	1.651855	0.327027	0.0292	0.358203	0.143746
0.000353	-0.6328	1.116706	0.289173	0.0219	16.8279	0.261728
0.000293	-1.56693	1.381829	0.250728	0.0146	1.2994	0.198454
0.000289	-0.5876	1.808	0.28016	0.04015	0.30295	0.131215

Min. Bot. Back.	Max. Bot. Back.	Avg. Bot. Back.	Min. Bot. CDOM	Max. Bot. CDOM	Avg. Bot. CDOM	Min. Bot. Chlor.
0.00022785	0.00067146	0.000328848	0.452	0.678	0.54798258	0.0365
0.0002821	0.0011067	0.000376303	0.4068	0.678	0.544173469	0.0584
0.00041664	0.00081747	0.000487819	0.452	0.6328	0.546183715	0.1022
0.00027528	0.00462024	0.000367371	0.2712	3.164	0.471797789	0.0219
0.00015438	0.00064728	0.000251593	0.3164	0.6328	0.520460271	0.0146
0.0001581	0.0016368	0.000303897	0.3616	0.678	0.534340313	0
0.00017298	0.00096534	0.000240786	0.2712	0.6328	0.521650656	0.0073
0.00013485	0.00238824	0.000583118	0.2712	0.693066667	0.528466372	0.0073
0.00017112	0.00125085	0.000258415	0.339	0.6328	0.469303898	-0.0073
0.00016461	0.00064635	0.000235901	0.2712	0.5424	0.442272821	-0.0073
0.00013392	0.000618347	0.00021352	0.0904	0.4972	0.364123112	-0.0803
0.00015159	0.00109554	0.000243006	0.1808	0.5424	0.369901567	-0.0073
0.0001612	0.003503811	0.000570403	0.226	0.8136	0.475140065	0.0073
0.00016554	0.003062304	0.00068125	0.2712	0.8136	0.504110585	0.0146
0.00017205	0.00054312	0.00028416	0.226	0.5876	0.428760917	0
0.00029574	0.001482523	0.000435171	0.210933333	0.5424	0.376004931	0.0073
0.00017856	0.0009486	0.000399336	0.3616	0.6328	0.485720647	-0.0073
0.0001829	0.00054312	0.000266219	0.1808	0.452	0.346192701	-0.0292
0.000185	0.000601	0.000285	0.0904	0.452	0.196867	-0.09125
0.000216	0.001287	0.000406	0.1808	0.5876	0.409056	-0.0365
0.000203	0.000796	0.000346	0.241067	0.5424	0.372918	0
0.000196	0.000784	0.000296	0.1808	0.452	0.35939	-0.0438
0.000182	0.000742	0.000295	0.226	0.9944	0.379042	0.0073

Max. Bot. Chlor.	Avg. Bot. Chlor.
0.43435	0.198777613
0.39055	0.155909715
0.41245	0.249099471
14.5197	0.25276924
0.3577	0.091087099
0.29565	0.04502701
0.4297875	0.05715997
0.5548	0.120749962
0.2482	0.037591485
0.5986	0.114677065
0.44165	0.087018128
0.3577	0.089004388
0.3139	0.095230924
0.2993	0.086238093
0.4818	0.100565861
0.4015	0.22525052
0.274966667	0.045525432
0.47085	0.059077393
0.513433	0.109151
0.37595	0.041021
1.14975	0.273333
0.68985	0.063181
0.574875	0.147511

Table E.4. The table shows average values for the surface (top 20 m) and bottom (last 20 m) layers for backscatter, CDOM, and chlorophyll for each season for when glider data is available. Units are none for backscatter, parts per billion (ppb) for CDOM, and μg/L for chlorophyll.

Averages	Surf. Back.	Surf. CDOM	Surf. Chlor.	Bot. Back.	Bot. CDOM	Bot. Chlor.
Spring 2022	0.000427469	0.524421407	0.313989296	0.000357321	0.545697113	0.173056874
Summer 2022	0.000328007	0.402486006	0.24811882	0.000370317	0.508850633	0.161080141
Fall 2022	0.000238437	0.285174911	0.133713309	0.000237083	0.408042053	0.082696041
Winter 2022/23	0.000291024	0.316867676	0.13999729	0.000448026	0.445515939	0.107120578
Spring 2023	0.000339736	0.123374158	0.136974529	0.000285385	0.196866966	0.109150748
Summer 2023	0.000327404	0.287010879	0.217858122	0.000345633	0.3772868	0.162614258
Fall 2023	0.000289181	0.280159558	0.131215066	0.000294853	0.379041683	0.147511118